The Journal of the Acoustical Society of America

An examination of point-particle Lagrangian simulations for assessing time-resolved hydroacoustic particle flux measurements in sediment-laden flows

Guillaume Fromant ; Peter D. Thorne ; David Hurther

Check for updates

View Online   Export Citation

JASA

ARTICLE

An examination of point-particle Lagrangian simulations for assessing time-resolved hydroacoustic particle flux measurements in sediment-laden flows

Guillaume Fromant,[1,a] (iD) Peter D. Thorne,[2] (iD) and David Hurther[3] (iD)

[1]*Laboratoire d'Informatique, Signal et Image de la Côte d'Opale, Université du Littoral Côte d'Opale, Calais, France*

[2]*National Oceanography Centre, Liverpool L3 5DA, Merseyside, United Kingdom*

[3]*Laboratoroire des Ecoulements Géophysiques et Industriels (LEGI), Université Grenoble Alpes, CNRS UMR 5519, Grenoble, France*

ABSTRACT:

Accurate modelling and prediction of sediment transport in aquatic environments is essential for sustainable coastal and riverine management. Current capabilities rely on physical process-based numerical models and fine-scale sediment flux measurements. High-resolution hydroacoustic instrumentation has emerged as a promising tool for such measurements. However, challenges arise due to the inherent complexity of ultrasound scattering processes. This study introduces a numerical modelling using a point-particle approach to simulate the echoes backscattered by such instrumentation in sediment-laden flow conditions. The model considers geometric, statistical, particle cloud, and flow-induced effects on sediment velocity, concentration, and flux estimates using an acoustic concentration and velocity profiler as a reference. The model performance is assessed here under unidirectional constant flow conditions in terms of velocity, concentration, and time-resolved sediment flux estimates for a large range of the particles' advection speed and sampled volume sizes. Application to the estimation of the measurement accuracy of sediment flux in these flows is also considered, with a final error on the flux seen to be partially controlled by the residence time of particles within the sampled volumes. The proposed model provides insights into scattering processes and offers a tool for investigating robust sediment flux estimation techniques in various flow conditions.

NOMENCLATURE

d_0	Distance between the emitter E and one of the two receivers R
β	Angle of orientation of the receivers compared to the vertical
γ	Angle formed by the emitter axis and the emitter–receiver axis
x, y, z	Cartesian coordinate system. The emitter and the two receivers are aligned in the yz plane
a, b	Receiver length, width
E, R_1, R_2	Location of the emitter, receiver 1 and receiver 2. The receiver position is symmetric with respect to the vertical axis of the coordinate system
F	Location of the focal point of the bistatic system
P_j	Coordinates of a particle j $(x_j, y_j, z_j)^T$
$\overrightarrow{V_j}$	Velocity vector of a particle j $(u, v, w)^T$
r_{1j}, r_{2j}	Distance between one particle at P_j and the emitter (subscript 1)/receiver (subscript 2)
r_0	Distance along the acoustic axis of the emitter to the point at which the sound pressure is A
$\overrightarrow{k_{Ij}}, \overrightarrow{k_{Sj}}$	Incident (I) and scattered (S) wave number relative to particle j
y_r, z_r	Position of one of the two receivers on the yz plane
θ	Angle formed between the vertical and the incident axis
θ_x, θ_y	Projection of the angle between the scattered axis and the receiver normal axis $\left(\overrightarrow{RF}\right)$ on the x and y planes
a_0	Emitter radius
D_E, D_R	Directivity functions of the emitter and receivers
ν	Emitter carrier frequency
A	Emitted pulse amplitude
τ	Emitted pulse duration
f_{PRF}	Pulse repetition frequency
t_{PRF}	$1/f_{PRF}$
f_e	Sampling frequency of the simulated echoes
R	Autocorrelation function
ρ	Normalized autocorrelation coefficient
α	$\sqrt{1 - \rho(t_{PRF})^2}$
s_v	Volume backscattering coefficient ($\mathrm{m^2.m^{-3}}$)
σ_j	Scattering cross section
$b(t)$	Recorded echo

a)Email: Guillaume.fromant@univ-littoral.fr

$S_a(t)$	Amplitude of the demodulated backscattered echo
$S_{a,rms}(t)$	Root mean square backscattered amplitude of the demodulated echoes
I, Q	In-phase and quadrature components of the Doppler signal obtained after demodulation of b(t)
η_I, η_Q	Noise terms in the in-phase and quadrature components I, Q
z_i	$I_i + jQ_i$
$\hat{\nu}_D$	Averaged Doppler frequency estimated with the pulse-pair method
ν_{Dj}	Doppler frequency shift induced by the motion of a particle at position P_j
ϕ	Phase of the demodulated backscattered echo
ϕ_i	Random phase of the return echo i from the N scatterers present in the sampled volume v_0
k	Range bin number
Ω_k	Volume covered by one pulse length centered around gate k position in bistatic configuration
v_0	Sampled volume at gate k
N	Number of particles in v_0
d_k, b_k	Distance of the gate k with respect to the emitter and one receiver
α_k	Doppler angle formed by the emitter axis and the line linking gate k to the receiver
m	Number of consecutive pulses considered in an estimate
P_n	Number of pulses generated in one simulation
N_s	Number of particles introduced in the simulation domain
t_p	Time separating two pulses
t^*	Time separating two pulses beyond which ρ drops below a value of 0.1 $[\rho(t^*) = 0.1]$
ρ_S	Particle density
a_p	Particle radius (m)
M	Mass concentration (kg.m^{-3})
c	Sound speed in water
α_w	Attenuation due to water

I. INTRODUCTION

Modelling and predicting sediment transport in aquatic environments is essential for reaching sustainable management of coasts and rivers. Our current capability to model sediment transport in the coastal or fluvial environments relies on a synergy between physical process-based numerical models, which are key for long term predictions of bathymetrical evolution under climate change scenarios, and fine-scale process measurements of sediment transport flows. This measurement ability appears as a crucial step in the validation of increasingly efficient turbulence-resolved two-phase flow simulations. This has led to the development of a variety of high-resolution instrumentation over the past 30 years for measurements of flow, particle, or sediment velocity [Pitot-tubes (Sumer *et al.*, 1996), conductivity probe (Pugh and Wilson,

1999)], sediment size and concentration [conductivity probes (Fromant *et al.*, 2018), capacity probes (Sumer *et al.*, 1996), gamma rays (Pugh and Wilson, 1999), or both particle velocity and concentration [image techniques (Capart and Fraccarollo, 2011; Spinewine *et al.*, 2011)], and active hydroacoustic techniques (Shen and Lemmin, 1997; Thorne and Hanes, 2002; Hay *et al.*, 2012a; Hurther *et al.*, 2011). The use of scattering based ultrasound has been one of the most promising candidates to non-intrusively observe the flow and sediment transport processes. In particular, they allow measurements of sediment fluxes in the benthic boundary layer as the product of pointwise measured particle velocity and concentration in highly turbulent geophysical flows, such as rivers, estuarine, and coastal ocean flows.

Mono- or multi-bistatic ultrasound sonars combining pulse-to-pulse coherent Doppler frequency profiling with incoherent backscattered intensity profiling can provide collocated time-resolved profiles (along the transmitted pulse direction) of multi-component velocity and sediment concentration. The use of MHz ultrasound frequencies in sediment-laden water flows allows to reach profiling ranges on the order of $\mathcal{O}$(m) with high spatial $[\mathcal{O}$(mm)] and temporal $[\mathcal{O}$(ms)] resolutions (Shen and Lemmin, 1997; Zedel and Hay, 1999; Hurther *et al.*, 2011; Hurther and Lemmin, 2001a; Zedel and Hay, 2002; Hurther and Thorne, 2011; Fromant *et al.*, 2018). In these sediment transport flows, typical sediment concentration values range from 0.01 to 1 g/l in the upper dilute suspension flow layer subject to turbulent particle motions, and from 10 to 1000 g/l in the lower dense bedload layer subject to collisional, saltating, rolling, or sliding particle motions. The corresponding flow opacity hinders the use of standard optical flow measurement tools, such as particle image velocity (PIV) or laser doppler velocimetry / laser doppler anemometry (LDV / LDA). Hydroacoustic measurement tools have offered an interesting means of high-resolution sediment flux estimates in boundary layer sediment transport flows (Revil-Baudard *et al.*, 2015; Fromant *et al.*, 2019; Naqshband *et al.*, 2021; Grossmann *et al.*, 2023) and, more recently, of direct comparison to novel turbulence-resolved two-phase fluid-particle simulations in sediment transport flows (Cheng *et al.*, 2018; Chauchat *et al.*, 2022).

Even though the basic measurement principles of hydroacoustic sediment flux measurements are well known and described in the literature (originally derived for radar interferometry applications) (Bamler and Hartl, 1998; Pepe and Calò, 2017), and medical applications (see Atkinson and Wells, 1977; Mo and Cobbold, 1992), data processing and analysis remains a challenge in aquatic environments due to the inherent complexity of ultrasound scattering processes. In particular:

(1) Sensor geometry of the system has strong effects on sediment flux measurements as it can result in range and velocity ambiguities (Hurther *et al.*, 2011; Hurther and Lemmin, 2001a; Zedel, 2008). Most specifically, the

Fromant *et al.*

10 June 2024 17:00:44

system geometry is crucial when it comes to multi-component velocity field estimation. In that sense, bistatic systems are preferred (Hurther and Lemmin, 2001a; Lhermitte and Lemmin, 1994; Zedel and Hay, 2002) but their intricate geometry complicates the estimation of particle concentration from the backscattered amplitude due to the range dependency of the sampled volumes, and associated loci and shape evolution with range and/or particle concentration (Zedel *et al.*, 2021).

(2) Hydroacoustic sediment flux measurements suffer from the dichotomy of requiring phase-coherent measurements of Doppler echo pairs (i.e., high temporal correlation of pulse pairs requiring the same particle population is insonified between consecutive echoes), and incoherent pulse echoes for concentration estimations, which requires statistical independency (absence of correlation between pulse echoes, that is, the particle population insonified between consecutive echoes differs). Indeed, phase-coherence from pulse-to-pulse is the essence for Doppler signal reconstruction and an estimate of the quasi-instantaneous particle velocity (Garbini *et al.*, 1982); hence, requiring high temporal resolutions via a high pulse repetition frequency (PRF). The opposite, phase incoherence, may be reached when consecutive echoes are no longer correlated, resulting in lower temporal resolutions for the backscattered amplitude (sediment concentration) estimation. This coherence/incoherence dichotomy partly explains the high uncertainties on time-resolved flux measurements in recent open-channel and field experiments. Thorne and Hurther (2014) addressed this aspect by measuring the characteristic Doppler correlation time scale in typical (highly turbulent) sediment transport flow conditions. This characteristic time scale was used to set the minimum time for statistical independence of consecutive pulse echoes. The number of (independent) pulse echoes used for the calculation of an acoustic intensity value determines the statistical bias error of a sediment concentration estimate. Thorne and Hurther (2014) showed that maximal bias errors of about 20% are obtained at measurement rates of around 8 Hz for sediment concentration profiles.

(3) A significant source of uncertainty also originates from the hydrodynamic flow regimes themselves, such as the level and the degree of isotropy of the flow turbulence within the sample volume [usually of the order of $\mathcal{O}(100\,\text{mm}^3)$], which can be seen as a source of incoherency that potentially decreases the temporal correlation of the Doppler signal. Other explicit noise sources, inherent to the measuring principle, such as the Doppler noise caused by the random velocity fluctuations of the scatterers within the sampling volume, also contribute to decorrelation (Garbini *et al.*, 1982; Voulgaris and Trowbridge, 1998; Hurther and Lemmin, 2001b).

In trying to improve hydroacoustic measurements of sediment fluxes, we need to better understand these geometric, statistical, and flow condition induced effects in order to better quantify the measurement accuracy of sediment velocity, concentration, and flux. In the present paper, a numerical modelling approach is presented to address this challenge, with the primary objective to simulate backscattered echoes with a point-particle approach to formulate any type of complex flows. This is key to elaborate new methods for processing and analyzing recorded echoes in complex turbulent flow conditions, and improve the quality of velocity, concentration, and flux measurements. Few other studies are based on a numerical modelling approach to simulate particle scattering processes, in particular for analyzing pulse-coherent Doppler velocity estimation. In the context of sediment transport, Zedel (2008) first proposed a numerical model capable of reproducing bistatic coherent Doppler backscatter from scattering fluid tracers in synthetic velocity fields. The model was recently improved in Zedel *et al.* (2021) to account for particle concentration, imposed as a mean intensity profile, and illustrates the evident synergy between simulations and measurements. For the latter numerical approach, the particle concentration is computed by approximating the integral over backscatter from individual sources through adjustments of a received backscattered level to achieve characteristic concentration profiles commonly observed above a moving bed in the bottom boundary layer of turbulent unidirectional flows (Eulerian approximation). This allowed circumvention of the high computational costs associated with large numbers of point-particle scatterers. Simulations in Dillon *et al.* (2012a) rather focused on reproducing the phase statistics of backscattered echoes using Monte Carlo simulations in an effort to elaborate noise reduction fusion filters for improved velocity estimation in the Bayesian framework, with no further consideration of the concentration profiles.

The present study uses an alternative approach based on a point-particle (in the Lagrangian sense) scattering model generating pulse-to-pulse coherent Doppler echoes recorded by bistatic systems, scattered by individual particles at a set volume concentration, and moving at a controlled unidirectional constant flow speed. This methodology provides more realistic estimates of the time-resolved (quasi-instantaneous) particle velocity, concentration, and fluxes obtained with commonly used bistatic systems. The present methodology strongly differs from previous numerical sediment fluxes estimates resulting from a continuum description of the sediment concentration. With this point-particle modelling approach, effects on the recorded pulse echoes will be investigated, due to beam pattern geometry, pulse carrier frequency, and pulse duration (as the control parameter of the sampled volumes size along the insonified water column), elementary particle scattering properties (via the prescription of the particle form function), spatial distribution of particles in the water column, and the imposed unidirectional constant particle velocity. The impact of these effects on measurement accuracy of time-resolved and mean sediment flux estimates will be quantified and discussed.

Fromant *et al.* 2819

10 June 2024 17:00:44

The modelled system depicted in the present paper is based on the characteristics of an acoustic concentration and velocity profiler (ACVP) technology (Hurther *et al.*, 2011). It is based on the ADVP technology proposed by Lemmin and Rolland (1997) as a multi-bistatic system using a high-directivity central transmitter with several wide-angle receivers to permit nearly collocated bistatic velocity measurements along a profile range aligned with the transmitting direction. Other multi-bistatic systems exist, such as the MFDop or Vectrino Profiler (Nortek Group, Trondheim, Norway) technologies of Zedel *et al.* (2021) or Thomas *et al.* (2017), respectively, using different sensors and sensor geometries. The ACVP geometry is deliberately chosen here due to its intensive implementation over the past 10 years in many coastal, river, open-channel, and wave-flume sediment transport studies (e.g., Fromant *et al.*, 2018; Fromant *et al.*, 2019; Grossmann *et al.*, 2022; Grossmann *et al.*, 2023; Naqshband *et al.*, 2014; Naqshband *et al.*, 2017; Naqshband *et al.*, 2021; Revil-Baudard *et al.*, 2015; Revil-Baudard *et al.*, 2016; van der Zanden *et al.*, 2016; van der Zanden *et al.*, 2018; Guta *et al.*, 2022). The results obtained herein apply to the simulated ACVP technology but other sensors and sensor geometries can be readily implemented.

The objective of this study is to assess the performance of proposed numerical model for simulations of hydroacoustic sediment transport measurements of sediment fluxes. As a first step in this novel numerical modelling approach, the case of particles moving at unidirectional constant speed (as an asymptotic case referring to the mean component of a turbulent flow) is tested and validated here before more complex turbulent sediment-laden flows will be considered in future studies. As a consequence, random scattering processes induced by flow turbulence are neglected, to isolate and identify the causes of ultrasound measurement uncertainty in sediment velocity, concentration, and sediment flux profiling.

The paper is organized as follows. Section II presents the considered sound scattering theory. Section III is devoted to the numerical implementation of the formulated scattering model. The simulation results are first assessed in terms of backscatter amplitude and particle velocity statistics (Sec. IV). Section V focuses on the simulated accuracy of sediment flux measurements. The conclusions are summarized in Sec. VI.

II. ACOUSTIC BACKSCATTER THEORY

A. Backscattered signal in bistatic configuration

We consider a multi-bistatic system (ACVP; Hurther *et al.*, 2011) (Fig. 1): the system is composed of one downward looking emitter and two receivers symmetrically positioned on either side of the emitter at a distance d_0, tilted by an angle $\beta = \pm 30°$ towards a point of intersection beneath the emitter. The angle formed by the emitter axis and the emitter–receiver axis is called γ. The emitter axis is aligned with the z axis. Both receivers are synchronized but record their own signal. For simplicity in the following, we'll focus
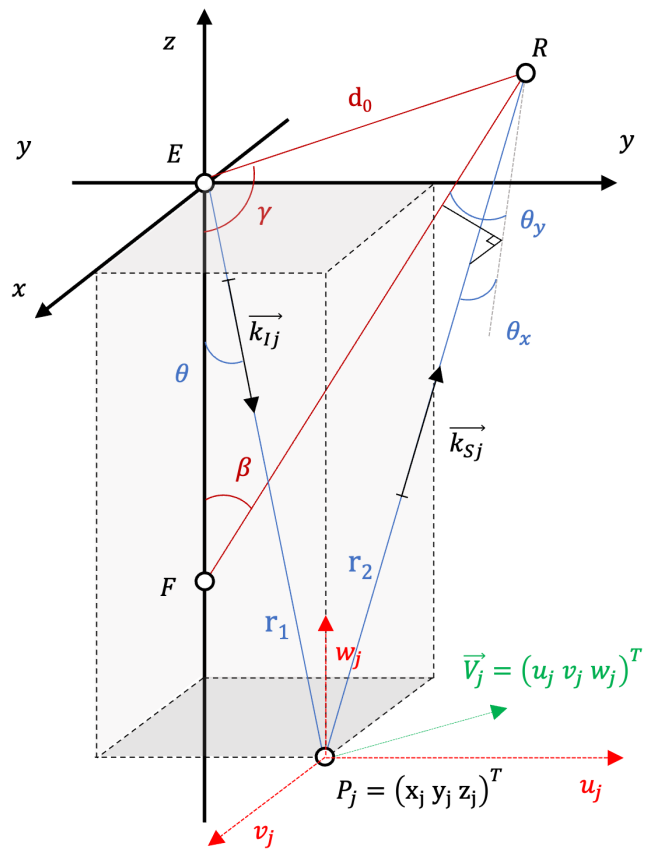

FIG. 1. (Color online) Schematics of the geometry adopted for the present simulation represented in a Cartesian coordinate system. The emitter (E) and receiver (R) are separated by a distance d_0. γ is the angle formed by the (ER) axis and the emitter normal axis (vertical axis here). The receiver normal axis points towards the focal point F of the system, forming a tilt angle β with the vertical axis. Each of the j particles are positioned at P_j, located at a distance r_{1j} from E and r_{2j} from R. Each particle moves at a velocity V_j. $\vec{k}_{Ij}$ and $\vec{k}_{Sj}$ are, respectively, the wave numbers of the pulse travelling the domain projected on the incident ($\overrightarrow{EP_j}$) and scattered directions ($\overrightarrow{P_jR}$). θ is the angle between the vertical axis and the incident axis. θ_x (θ_y) is the projection of the angle between the scattered axis and the receiver normal axis ($\overrightarrow{RF}$) on the x (y) plane.

on a single emitter–receiver couple forming one of the two bistatic subsystems of the ACVP. The emitter is a circular piston transducer of radius a_0, and the receiver is rectangular with a length a and a width b (see Fig. 2; with $a \gg b$ so that the beam opening is wide in the vertical plane (elevation) and narrow in the horizontal plane (azimuth).

The pulses are modelled as sine waves of carrier frequency ν, amplitude A, and duration τ, emitted at a pulse repetition frequency f_{PRF} on the order of kHz:

$$s(t) = A \cdot \sin(2\pi\nu t) \cdot rect(t, \tau). \tag{1}$$

The rect function here represents a gated unit rectangle function of duration τ. In the following, the filtering effect due to the sensor bandwidth is not taken into account in the numerical model.

The pulse travels within the flow domain below the emitter and is scattered by each insonified particle P_j present in the domain. The water-sediment mixture is treated as a
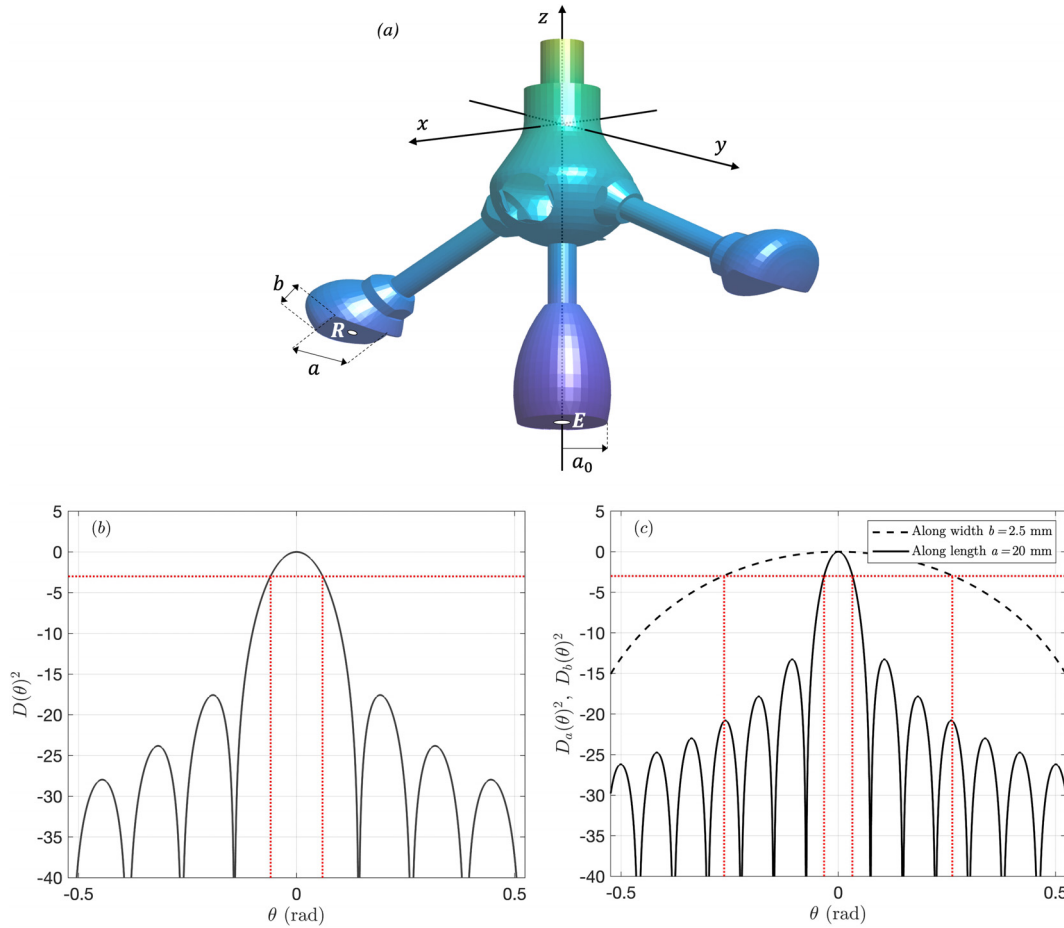
FIG. 2. (Color online) (a) Three-dimensional (3D) view of the ACVP transducers composed of one central emitter E and two symmetrical receivers R_1 and R_2, (b) directivity patterns of the circular emitter, (c) directivity patterns of the rectangular receivers split along the transducer width b (dashed black line) and length a (solid black line) of the model system. The dotted red lines represent the -3 dB threshold and the corresponding angles are indicted with the red dotted lines.

dilute suspension (i.e., *with* a mean volumetric sediment concentration below 10%), so that sound attenuation due to particle scattering or sediment viscous effects can be ignored. After reaching a particle P_j, a component of the scattered wave is directed towards the bi-static receivers; this we refer to as the backscattered component. The wave travel time from its emission to its reception equals $(r_{1j} + r_{2j})/c$, r_{1j} (and r_{2j}) being the distance between the emitter (receiver) and the particle P_j. The recorded echo, $b(t)$, finally consists of the summation of all the individual backscattered echoes from each of the N particles within the insonified volume:

$$b(t) = \sum_{j=1}^{N} \frac{A D_j \sqrt{\sigma_j}}{r_1 r_2} \sin\left(2\pi[\nu + \nu_{Dj}]\left[t - \frac{r_{1j} + r_{2j}}{c}\right]\right)$$
$$\cdot e^{-\alpha_w(r_1 + r_2)} \cdot rect\left(t, \frac{\tau \nu}{\nu + \nu_{Dj}}\right), \qquad (2)$$

where, α_w is the attenuation coefficient due to water, σ_j is the scattering cross section of particle P_j (set constant in the simulations), ν_{Dj} is the Doppler shift induced by the motion

of particle P_j following the velocity vector $\overrightarrow{V_j} = (u\,v\,w)^T$ ($.^T$ is the transpose operator), c is the speed of sound in water. Placing the frame origin at the emitter, the positions of the emitter and the receiver are set to $E = (0, 0, 0)^T$ and $R = (0, y_r, z_r)^T$. Given a particle P_j with coordinates $(x_j\,y_j\,z_j)^T$ in the domain, we define the following vectors, respectively, aligned with the incident direction (emitter-particle direction, subscript I) and scattering direction (particle-receiver direction, subscript S):

$$\overrightarrow{k_{Ij}} = \frac{2\pi\nu}{c}\begin{pmatrix} x_j \\ y_j \\ z_j \end{pmatrix} \cdot \frac{1}{r_{1j}}, \quad \overrightarrow{k_{sj}} = \frac{2\pi\nu}{c}\begin{pmatrix} -x_j \\ y_r - y_j \\ z_r - z_j \end{pmatrix} \cdot \frac{1}{r_{2j}}. \qquad (3)$$

The Doppler shift ν_{Dj} is then determined as the scalar product between $\overrightarrow{V_j}$ and $\overrightarrow{k_{sj}} - \overrightarrow{k_{Ij}}$:

$$\nu_{Dj} = \frac{1}{2\pi}\overrightarrow{V_j} \cdot \left(\overrightarrow{k_{sj}} - \overrightarrow{k_{Ij}}\right). \qquad (4)$$

$D_j = \sqrt{D_E^2 * D_R^2}$ in Eq. (2) is the range-dependent directivity function of the system (root mean square product of the range-independent directivity functions of the circular

J. Acoust. Soc. Am. **155** (4), April 2024

Fromant *et al.*   2821

piston emitter D_E of radius a_0 and the rectangular receiver D_R of length a and width b evaluated at the location of the particle P_j (Fig. 1):

$$D_E(\theta) = \frac{2J_1(ka_0\sin(\theta))}{ka_0\sin(\theta)}, \tag{5}$$

$$D_R(\theta_x, \theta_y) = \frac{\sin\left(\frac{b}{\lambda}\sin(\theta_x)\right)}{\frac{b}{\lambda}\sin(\theta_x)} \cdot \frac{\sin\left(\frac{a}{\lambda}\sin(\theta_y)\right)}{\frac{a}{\lambda}\sin(\theta_y)}. \tag{6}$$

θ_x and θ_y are functions of the receiver position and its tilt angle β relative to the vertical axis. For a standard ACVP configuration, such as described in Hurther *et al.* (2011) and Fromant *et al.* (2018), $a_0 = 6.35$ mm, $a = 20$ mm, and $b = 2.5$ mm.

The volume v_0 sampled by one receiver at range bin k corresponds to the integral of the squared directivity function of the system D^2 over the volume Ω_k covered by one pulse length. In bistatic configuration, Ω_k is the volume enclosed within the two ellipsoidal surfaces, taking their foci at the emitter and receiver, representing the iso-travel paths of the wave from the emitter to the receiver at the beginning and end of the pulse. For typical systems (Hurther *et al.*, 2011; Moore and Hay, 2009; Zedel *et al.*, 2021), the sampled volumes are on the order of $\mathcal{O}(100\,\mathrm{mm}^3)$.

The amplitude [$S_a(t)$] and phase (ϕ) of the demodulated backscattered signal, respectively, enable estimates of the concentration and the velocity. While the velocity estimation relies on the coherence existing between two pulsed echoes sufficiently close in time and insonifying the same cloud of scatterers in motion, this is not the case for the concentration, for which consecutive pulses need to be decorrelated statistically as incoherent. Due to the random spatial distribution of the N particles within the sampled volume, the backscattered amplitude of two particle clouds, between consecutive insonifying pulses, with similar particle numerical densities but different spatial distributions, will vary due to the random phase ϕ_i of the return echoes from the N scatterers [Eq. (7); Strutt and Rayleigh, 1877]. As multiplying the number of observations of the backscattered amplitudes using multiple pulses m, the phase terms in Eq. (7a) below become uniformly distributed between 0 and 2π with a zero-value average over m echoes (consecutive or not). Thus, the root mean square of Eq. (7a) over m echoes, $S_{a,rms}(t)$ [Eq. (7b)], tends towards $\sqrt{N}$ as the number of pulses increases, since the random position of the particles in the flow changes as they pass in and out of the insonified volume,

$$S_a(t) \propto \sqrt{N}\left(1 + \frac{2}{N}\sum_{n=1}^{N}\sum_{p \neq n}\cos(\phi_n - \phi_p)\right)^{1/2}, \tag{7a}$$

$$S_{a,rms}(t) = \sqrt{\frac{1}{m}\sum_{i=1}^{m}S_a(t_i)^2} \propto \sqrt{N}. \tag{7b}$$

B. Coherent velocity estimate

In practice, the recorded signal at a receiver, $b(t)$, is demodulated by the carrier frequency ν to obtain the in-phase (I) and quadrature (Q) components (for distinction of velocity direction) of the Doppler signal at range gate k:

$$I = \int_0^{t_{PRF}} b(t)\sin(2\pi\nu t) \cdot rect\left(t - \frac{d_k + b_k}{c}, \tau\right)dt$$
$$= \frac{A \cdot S_a(t)f_e\tau}{2}\cos(\phi) + \eta^I, \tag{8}$$

$$Q = \int_0^{t_{PRF}} b(t)\cos(2\pi\nu t) \cdot rect\left(t - \frac{d_k + b_k}{c}, \tau\right)dt$$
$$= \frac{A \cdot S_a(t)f_e\tau}{2}\sin(\phi) + \eta^Q. \tag{9}$$

η^I and η^Q are a combination of noise terms (Doppler noise, system noise, thermal noise, etc.) decorrelating the in-phase and quadrature components, d_k is the vertical position of the gate of interest on the emitter axis, and b_k is the distance between the gate k and the receiver. Here, $\phi = 2\pi\nu_D t$, where ν_D is the Doppler frequency seen at the receiver, f_e is the sampling frequency of the recorded signal, and $S_a(t)$ is the amplitude of the backscattered signal. $f_e\tau$ samples are summed over a total duration of $t_{PRF} = 1/f_{PRF}$ to produce I and Q at gate k.

The autocorrelation function R (and its normalized equivalent ρ) can then be estimated from a finite sequence $z_1...z_m$ corresponding to an ensemble of m consecutive pulses ($z_i = I_i + jQ_i$), the emissions of which are separated by a time t_p,

$$R(t_p) = E\left(z_i^*z_{i+1}\right) = \frac{1}{m-1}\sum_{n=1}^{m-1} z_n^*z_{n+1}, \tag{10a}$$

$$\rho(t_p) = \left|\frac{R(t_p)}{R(0)}\right|$$
$$= \left|\frac{1}{m-1}\sum_{n=1}^{m-1} z_n^*z_{n+1}\right| \bigg/ \frac{1}{m-1}\sum_{n=1}^{m-1}|z_n^*z_{n+1}|, \tag{10b}$$

where $*$ denotes complex conjugation. The autocorrelation function of the complex signal being itself complex, the normalized autocorrelation function $\rho(t_p)$ offers the benefit of taking values between 0 and 1 to express the degree of correlation between pulses (Dillon *et al.*, 2011; Zedel *et al.*, 1996). For small t_p (i.e., $t_p = t_{PRF} = 1/f_{PRF}$), ρ is the highest and monotonically decreases towards 0 as t_p, the time elapsed between two pulses, increases. For pulsed sonar systems, the smallest value of t_p is $t_{PRF} = 1/f_{PRF}$. $\rho(t_{prf})$ is also called the autocorrelation coefficient.

An average Doppler frequency estimate $\hat{\nu}_D$ at each receiver can then be determined from the time derivative of the phase (divided by 2π) of the pulse-to-pulse autocorrelation function $R(t_p)$ using m consecutive pulses with the pulse-pair method (Lhermitte and Serafin, 1984). Therefore,

if $t_p = t_{PRF}$ is the time elapsed between two consecutive samples, and m is the number of samples over which $R(t_p)$ has been averaged [see Eq. (10a)], in the pulse sequence, one writes

$$\hat{\nu}_D = \frac{1}{2\pi t_{PRF}} \arctan\left(\frac{Im(R(t_{PRF}))}{Re(R(t_{PRF}))}\right) \qquad (11)$$

because for $t_p = 0$, the phase of $R(t_p = 0)$ is equal to zero, by definition. This method is the most robust method against noise terms η (Lhermitte and Serafin, 1984). Using two receivers R_1 and R_2, respectively located right and left of the emitter, the 2-component velocity at range bin k can further be estimated by simple geometric transformation with prior knowledge of the Doppler angle α_k at range bin k (angle between the emitter normal axis and the range bin-receivers axis):

$$\begin{cases} u = \dfrac{c}{2\nu \sin(\alpha_k)} (\nu_{D_{R_1}} - \nu_{D_{R_2}}), \\ w = \dfrac{c}{2\nu(1 - \cos(\alpha_k))}(\nu_{D_{R_1}} + \nu_{D_{R_2}}). \end{cases} \qquad (12)$$

The pulse-pair phase (velocity) distribution is well known in the synthetic aperture radar (SAR) literature. The resulting distribution is a highly non-linear symmetric function of the phase difference $\psi = \hat{\phi} - \phi_k$ (Bamler and Hartl, 1998; Dillon *et al.*, 2012b). In the limit of $\rho \to 1$, the behavior of this function can be shown to be a Pearson type VII distribution of the form

$$p(x) = \frac{\Gamma(\mu)}{\zeta\sqrt{\pi}\Gamma\left(\mu - \frac{1}{2}\right)} \left[1 + \left(\frac{x}{\zeta}\right)^2\right]^{-\mu}, \qquad (13)$$

with parameters μ and ζ given by $\frac{3}{2}$ and $\sqrt{1 - \rho^2}$, respectively, and Γ being the Gamma function.

C. Incoherent concentration estimate

The backscatter amplitude S_a recorded by a receiver can be estimated from the in-phase and quadrature components of the Doppler signal:

$$S_a = \sqrt{\left(\frac{2I}{f_e\tau}\right)^2 + \left(\frac{2Q}{f_e\tau}\right)^2}. \qquad (14)$$

S_a is linked to the particle number N within the sampled volume [Eq. (7)]. However, the phase terms in Eq. (7a) prevent direct estimation of $\sqrt{N}$. Due to the stochastic nature of the backscatter amplitude [Eq. (7)], the root mean square backscatter is thus computed over an ensemble (or sequence) of m backscattered amplitudes following a Rayleigh distribution (Strutt and Rayleigh, 1877), ensuring the phase of the signal is uniformly distributed over 2π. In its time-discretized form, Eq. (7b) then gives

$$S_{a,rms} = \sqrt{\frac{1}{m}\sum_{i=1}^{m} S_{a_i}^2}. \qquad (15)$$

Using the wave equation, the backscatter can be normalized by the sampled volume to obtain a volume backscattering coefficient (m^2/m^3)

$$s_v = \frac{S_{a,rms}^2}{A^2 r_0^2} \bigg/ \iiint_V \frac{D_E^2 D_R^2}{r_1^2 r_2^2} e^{2\alpha(r_1+r_2)} dv. \qquad (16)$$

With α, an attenuation term containing attenuation effects due to water and sediment (the latter is neglected in the present case), r_0 is the distance along the acoustic axis of the emitter to the point at which the sound pressure is A, and v_0 is the sampled volume, a function of the pulse length τ and range. Under the assumption of incoherence, s_v can be related to the particle number N within the volume v_0, with prior knowledge of the scattering cross section $\sigma \, (m^2)$ for a particle of radius a_p and density ρ_s. For the simulations, all particles were identical in size. We also assume here that under the assumption of Rayleigh scattering (radius of the particles $a_p \ll \lambda$ the wavelength), the variation of σ according to the scattering angle can be ignored (Moore and Hay, 2009). We thus consider scattering to be isotropic around the backscatter direction and use the backscattering cross section $\sigma_{bs} = \sigma(\theta = -pi)$ to describe the particles scattering properties:

$$\frac{N}{v_0} = \frac{s_v}{\sigma_{bs}} = \frac{3M}{4\rho_s\pi a^3}, \qquad (17)$$

where M kg.m^{-3} is the particle mass concentration.

III. SIMULATION DESIGN

Several simulations were carried out to assess the model capability to return consistent velocity and concentration estimates. The standard system geometric configuration is that of an ACVP system ($d_0 = 69.3$ mm; $\gamma = 133.5°$ rad; $\beta = 30°$) (Fromant *et al.*, 2018; Hurther *et al.*, 2011). In all simulations, further referred to as runs, temporal signals are sampled at a frequency $f_e = 100$ MHz. In each run, P_n [$O(10^4)$] pulses of duration τ with a carrier frequency $\nu = 1$ MHz are emitted at a pulse repetition frequency $f_{PRF} = 1600$ Hz, and $b(t)$ [Eq. (2); see Fig. 3] is continuously computed and stored for each of the two receivers. N_s particles are introduced in a 7×10^5 mm^3 rectangular domain ($x = y = -50$–50 mm, and $z = 60$–130 mm) surrounding the system range-dependent directivity patterns highlighted in Fig. 4, the position of which being uniformly distributed along the x, y and z axis. This domain was chosen to cover a major part of the system directivity patterns in the far field of the system, centered around $z = 95$ mm from the emitter. Each particle in the domain is given the same advection speed, here in a direction aligned with the yz plane, with velocities varying between 0.1 and 1 m/s between runs. While it was possible to include turbulence in the present model, no turbulent fluctuations of the particle velocity were introduced for the purpose of this study devoted to model performance assessment in unidirectional constant flow. For these constant velocity values, no aliasing effect occurs over
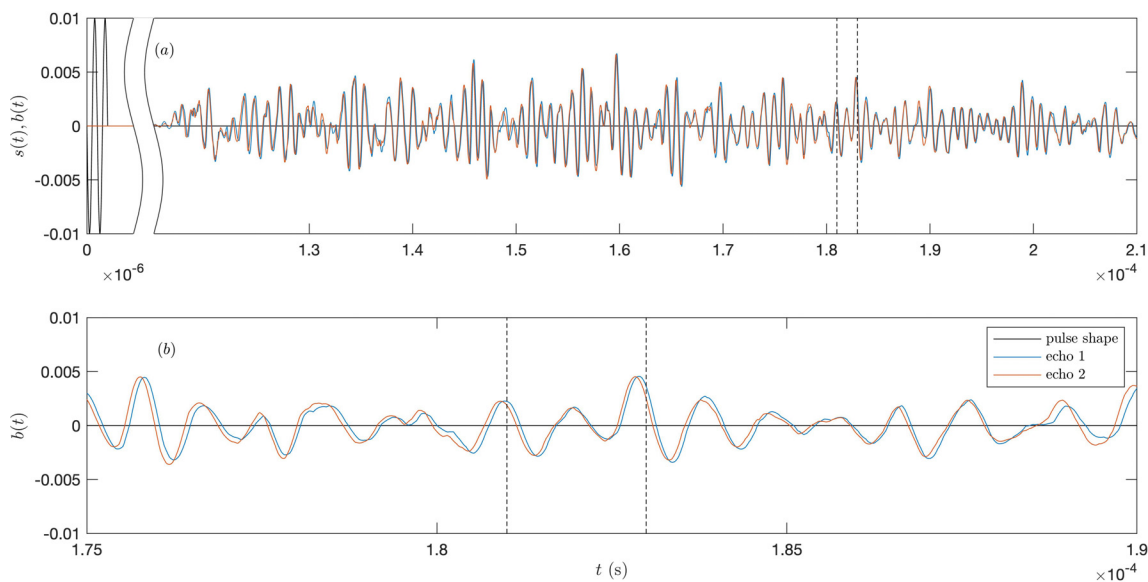
J. Acoust. Soc. Am. **155** (4), April 2024

Fromant *et al.* 2823

FIG. 3. (Color online) (a) s(t), the 2 μs sinusoidal pulse emitted at 1 MHz and associated echo. Blue and orange lines represent two consecutive pulses simulated for particles moving in the positive y direction with an advection velocity of 0.5 m/s (run 3, Table I). (b) Closeup of the echo centered around the range bin of interest (dashed vertical lines) at a vertical position $z = 0.1079$ m.

the entire profiling range. The number of particles was set to reach numerical densities of 2.86×10^7 particles per unit m^3, thus accounting for 2×10^4 particles in the simulation domain, for a corresponding volume concentration of 1.2×10^{-4} m^3/m^3. This value has been chosen to maintain a constant non-zero pulse-to-pulse number of particles (hence, instantaneous volume concentration) within the volumes sampled by the ACVP system, which is on the order of $\mathcal{O}(100 \, \text{mm}^3)$ using a standard geometric bistatic configuration

as described above (In these conditions, around three particles are located within the –3 dB sampled volume on average. Note that the total backscatter is from the whole insonified volume containing sufficient particles for Rayleigh statistics to apply.) This number was never perfectly constant due to the random spatial distribution of the particles within the flow region. Furthermore, this volume particle concentration value of 1.2×10^{-4} ensures dilute particle suspension conditions for which particle scattering induced attenuation
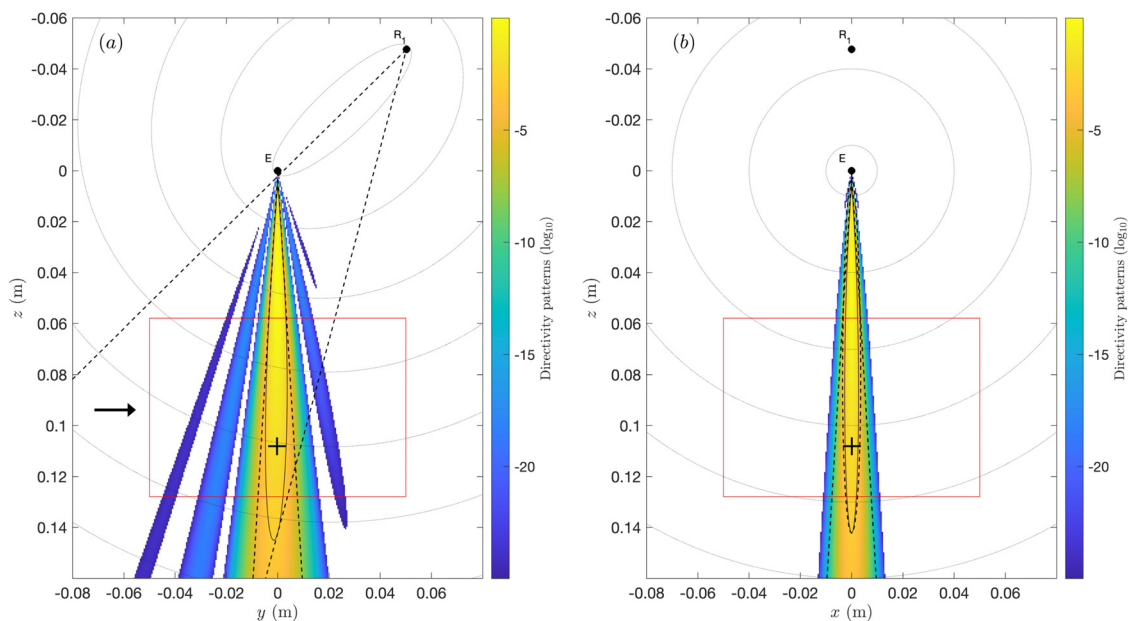

FIG. 4. (Color online) Spatial directivity patterns of the modelled system in (a) the yz plane and (b) the xz plane. The red boxes indicate the limits of the domain in which particles are in motion. The dotted lines define the –3 dB limits of the directivity patterns of the emitter E and one receiver R_1 projected on (a) the yz plane and (b) the xz plane. The solid black line is the –3 dB contour of the complete system directivity patterns. Here, $d_0 = 69.3$ mm, $\gamma = 133.5°$, $\beta = 30°$, $a_0 = 6.35$ mm, $a = 20$ mm, $b = 2.5$ mm. The emitter is located at (0,0,0), the receiver is located at (0,0.05, –0.045). The black arrow shows the flow direction, the black + shows the range gate of interest at $z = 107.9$ mm from the emitter.

2824   J. Acoust. Soc. Am. **155** (4), April 2024
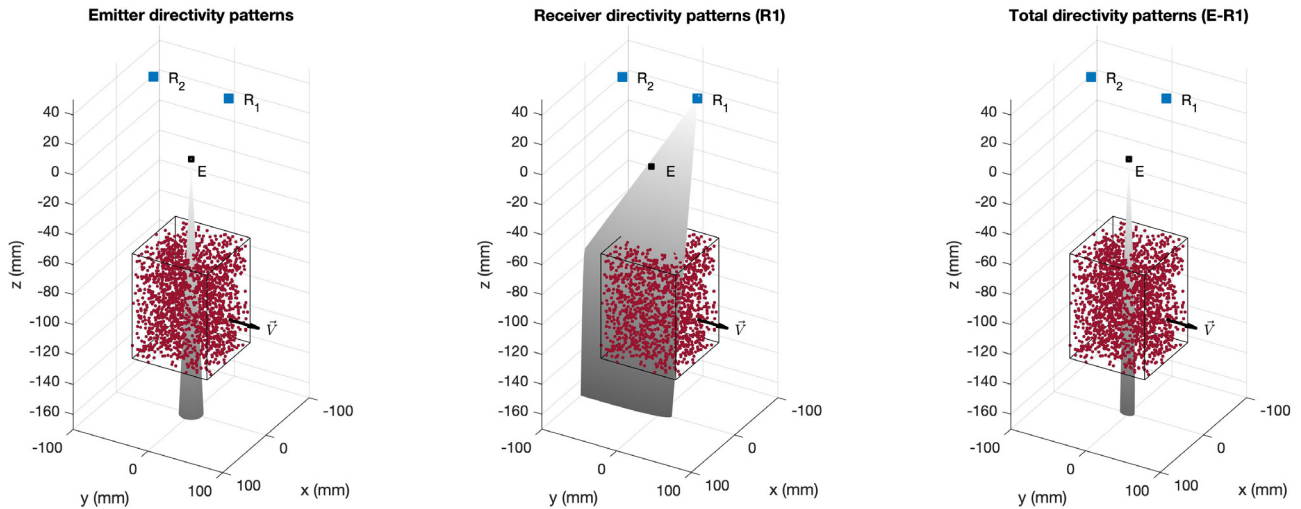
Fromant *et al.*

FIG. 5. (Color online) 3D representation of the sampled domain and transducers' sensitivities for the emitter E (left), receivers $R1$ and $R2$ (middle), and directivity patterns of one emitter–receiver couple (right). The red dots are modelled particles moving at an advection speed $\vec{V} = (0, v, 0)^T$. The gray regions (isocontours) bound the mainlobe of the emitter E (left panel), the receiver $R1$ (middle panel), and the couple emitter–receiver E–R1 directivity functions (right panel). These regions illustrate the volume sampled within the simulated domain bounded by the rectangular box.

remains negligible. Each particle possesses scattering properties close to that of a spherical sand particle ($\rho_s = 2650 \, \text{kg.m}^3$) of radius $a_p = 100 \, \mu\text{m}$, with a backscattering cross section $\sigma_{bs} = 8.70 \times 10^{-11} \, \text{m}^2/\text{m}^3$ (Thorne and Hanes, 2002). A 3D view of the way system directivity patterns intersect the simulation domain is shown on Fig. 5.

The present simulations allowed the control of the sampled volume by two means. The pulse length was varied between 2 and 12 μs, leading to changes in the sampled volume along the vertical axis, and the emitter directivity patterns, controlled through the circular piston radius a_0, were selected to be between 2.12 and 19.05 mm. The latter influenced the volume size as well as its aspect ratio. These cases with varying sampled volumes are not necessarily practical configurations; they were chosen to illustrate the impact of volume changes in the present case of unidirectional constant flow test conditions. Although the synthetic echoes covered a spatial range on the order of the vertical size of the simulation domain, all the velocities and concentration estimates studied hereafter only concern one range gate centered at $z = 107.9$ mm below the emitter and located in the sensor far field (marked as a black + on Fig. 4).

Several parameters were also stored so that there was access to each particle position/velocity within the domain. All these parameters were computed in the gate of interest at d_k ($z = 107.9$ mm) for both receivers, such as the number of particles present within the mainlobe of the directivity patterns of the system, the actual velocity of each particle within the beam (that is the same for each particle) and the particle velocity observed by the system after projection on the sampled volume phase center.

Table I lists the runs that were carried out and the associated relevant input parameters. Each run was launched on a clustering machine and lasted approximately 15 h to generate $P_n = 10^4$ raw backscattered echoes [Eq. (2)].

IV. SIMULATION ASSESSMENT

In the following, the model performance is evaluated based on simulated backscattered echo amplitudes and phases, for various particle advection speeds and different settings of sampled volumes under unidirectional constant flow conditions. For each simulation, a uniform concentration with randomly distributed particles is set in the

TABLE I. Summary of the simulation runs. For all runs, the PRF was set to 1600 Hz, the number of particles per unit m^3 was set constant to 2.86×10^7, and the center of the sampled volume investigated here is set to $d_k = 107.9$ mm. The particle scattering properties were the same in all runs, as well as the geometric properties of the system ($d_0 = 69.3$ mm; $\gamma = 133.5°$ rad; $\beta = 30°$) and the receivers' dimensions $(a, b) = (20, 2.5)$ mm. Note that Runs 1–9 and 16–18 possess a standard ACVP system geometry configuration such as described in Sec. II A. Also, note that u, v, w are the particles velocity components aligned with the x, y, z coordinates, respectively.

Run	P_n	u, v, w (m/s)	τ (μs)	a_0 (mm)	Sampled vol. (-3 dB) (mm^3)
1	10 000	(0,0.1,0)	2	6.35	108.8
2	10 000	(0,0.25,0)	2	6.35	108.8
3	10 000	(0,0.5,0)	2	6.35	108.8
4	10 000	(0,0.75,0)	2	6.35	108.8
5	10 000	(0,1,0)	2	6.35	108.8
6	10 000	(0,0.5,0)	4	6.35	217.1
7	10 000	(0,0.5,0)	6	6.35	325.4
8	10 000	(0,0.5,0)	8	6.35	434.1
9	10 000	(0,0.5,0)	12	6.35	651.5
10	10 000	(0,0.5,0)	2	12.7	36.5
11	10 000	(0,0.5,0)	2	9.52	59.4
12	10 000	(0,0.5,0)	2	19.05	17.4
13	10 000	(0,0.5,0)	2	3.18	251.9
14	10 000	(0,0.5,0)	2	4.23	182.0
15	10 000	(0,0.5,0)	2	2.12	385.3
16	80 000	(0,0.1,0)	2	6.35	108.8
17	80 000	(0,0.5,0)	2	6.35	108.8
18	80 000	(0,0.75,0)	2	6.35	108.8

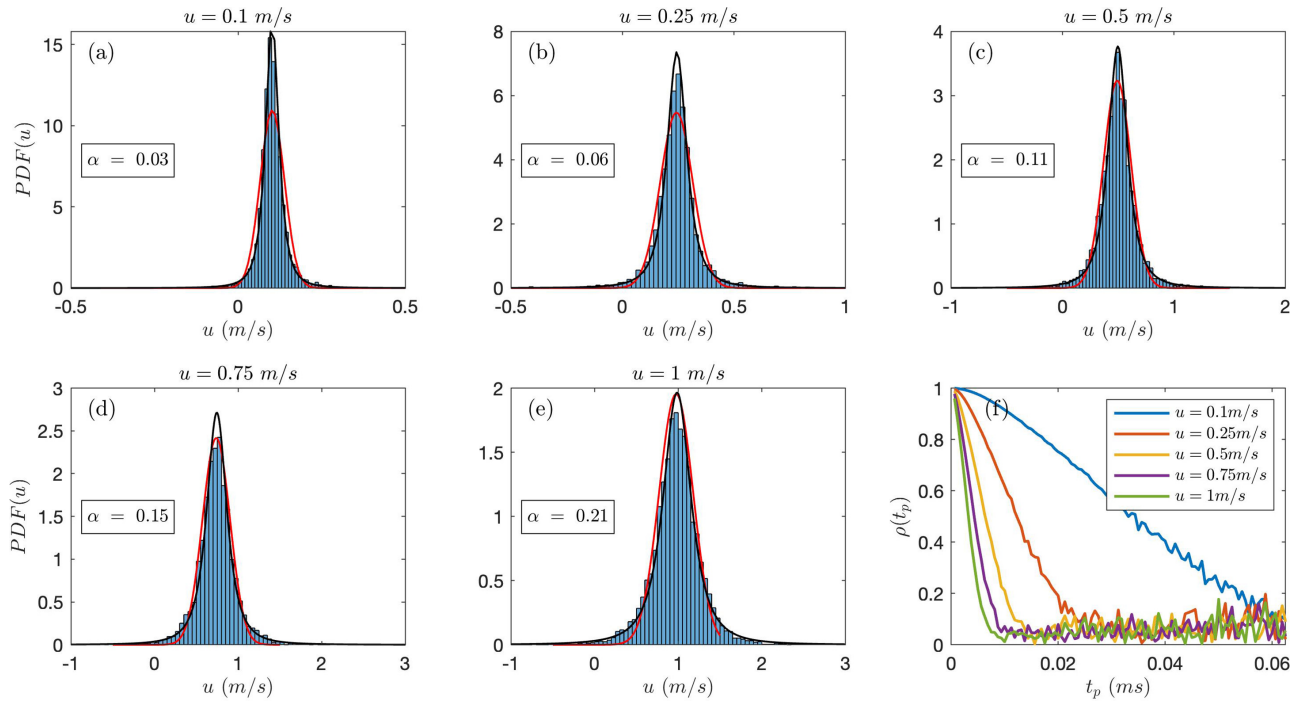J. Acoust. Soc. Am. **155** (4), April 2024

Fromant *et al.*   2825

FIG. 6. (Color online) (a)–(e) PDF(v) of the instantaneous velocities (using two consecutive pulses) for various velocities (Runs 1–5) and fixed sampled volume. The red lines are normal fits to the distributions shown here as a reference, the black lines are Pearson type VII fits to the distribution. (f) Normalized autocorrelation function of the estimated velocity time series for all velocity cases, t_p, is the time elapsed between two pulses.

simulation domain. The particles are further advected at a constant speed normal to the emitter axis and aligned to the emitter–receivers plane in the y direction with velocity v. The particle mass concentration (proportional to the number of particles per unit volume for a fixed a_p) is set constant in time within the simulation domain, in the sense that each particle leaving the simulation domain at one face is reintroduced within the simulation domain at the opposite face at a random position over the face surface—this to avoid periodicity effects of the simulation. The potential of the present model to reproduce numerically consistent velocity, concentration, and sediment flux measurements is discussed in this section.

A. Controlling particle advection speed

Figure 6 presents the histograms of instantaneous particle velocity estimated using two consecutive pulses [$m = 2$ in Eqs. (10a) and (11) to compute the pulse-pair velocity estimate] for the case of varying particle advection speed (Table I, Runs 1–5; Fig. 6). The estimated horizontal velocities were computed using both receivers' echoes, according to Eq. (12). Despite the constant particle advection speed, the estimated velocity shows random fluctuations. This is due to the Doppler spectrum spreading induced by the random phase distribution of the backscattered echo as the particles move through the sampled volume. The velocity reconstruction obtained using Eq. (12) assumes identical positions (on the emitter axis) of all scatterers within the sampled volume whereas spatial deviations from the assumed position exist leading to random fluctuations in the computed velocities. The estimated velocities are distributed

following a Pearson type VII distribution, Eq. (13) (a normal fit to the distributions is also displayed as a reference in Fig. 6). This is in accordance with previous results derived from radar interferometry in bistatic configuration (Pepe and Calò, 2017). The width of the distribution is controlled by the parameter $\alpha = \sqrt{1 - \rho(t_{PRF})^2}$, where $\rho(t_{PRF})$ is the normalized autocorrelation function computed following Eq. (10a) based on the demodulated echoes seen at one of the two receivers (the result is similar for each receiver). α increases with increasing advection speed [Figs. 6(a)–6(e)], associated with a decrease in peak value of PDF(v), highlighting the fact that the correlation coefficient between consecutive samples tends to decrease with increasing advection speed in the absence of any turbulent particle motions.

This is further illustrated on Fig. 6(f), where the normalized autocorrelation function of the velocity time series is seen to decrease more rapidly in time with increasing particle advection velocity. This trend was anticipated as the particle population (more particularly their spatial distribution) within the sampled volume changes more rapidly in-between consecutive pulses emitted at a constant PRF (here of 1600 Hz) as the particle advection speed is increased. A reasonable hypothesis indeed considers that consecutive pulses remain correlated as long as the same particle population is insonified within the sampled volume. In the present case of unidirectional constant flow conditions, at fixed sampled volume size, only the particle advection speed controls the residence time of a particle cloud within the sampled volume.

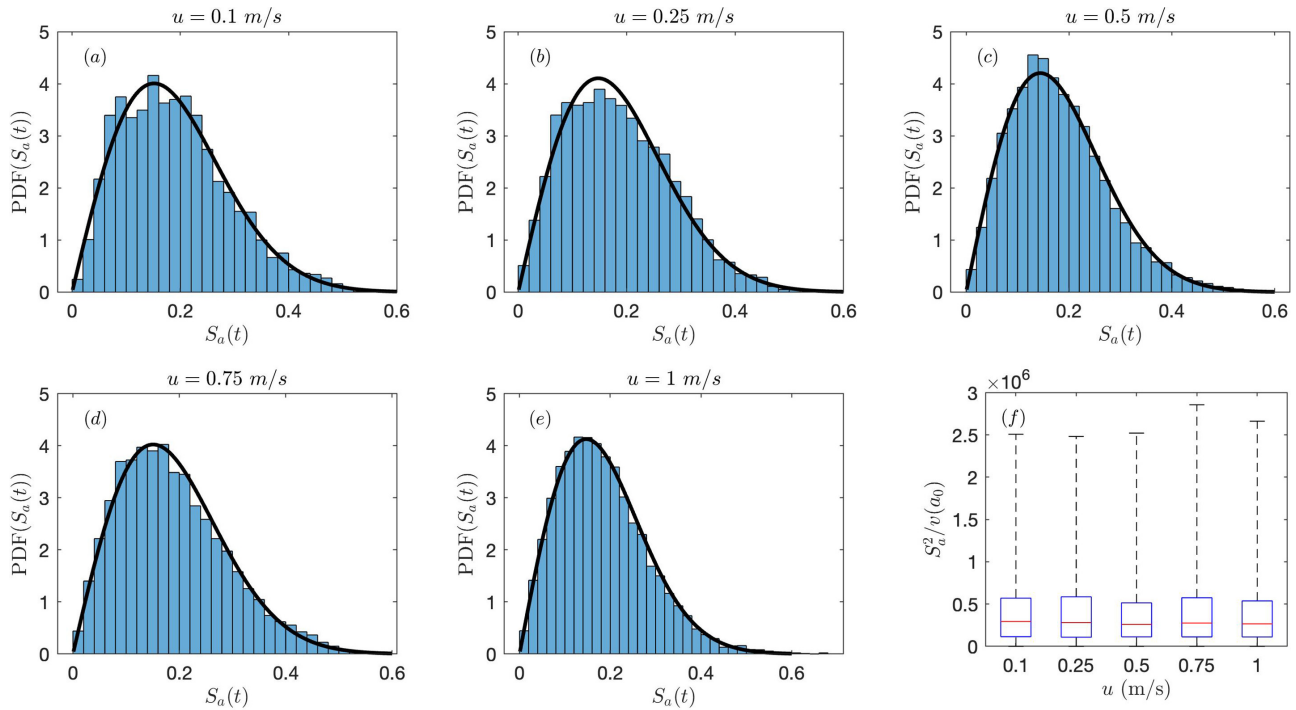For all these runs, backscattered signal amplitudes $S_a(t)$, Eq. (14) histograms were also computed for different

2826   J. Acoust. Soc. Am. 155 (4), April 2024

Fromant *et al.*

FIG. 7. (Color online) (a)–(e) PDF($Sa(t)$) of the backscattered amplitudes for particle advection velocities ranging from 0.1 to 1 m/s (Runs 1–5). The black lines are the Rayleigh fits to the distributions. (f) Boxplots representation of the mean squared backscatter distributions for all advection velocities where the red lines represent the median value, and the extrema of the dotted lines show the extrema of the distribution. The upper and lower levels of the boxes in the boxplot refer to the 25th and 75th percentiles.

advection speeds (Table I, Runs 1–5; Fig. 7). Time series of $S_a(t)$ are Rayleigh distributed as expected (Strutt and Rayleigh, 1877; Zedel, 2008), displaying similar mean square values [Fig. 7(f)] normalized by the sampled volume $v_0(a_0)$ (in m^3). The width of the distributions appears steady as shown in Fig. 7(f) where $S_a^2(t)/v_0(a_0)$ exhibit similar median and $\frac{1}{4}$ and $\frac{3}{4}$ quantiles.

B. Controlling volume size and shape

The present model also allows control of the sampled volume size, by modifying the pulse length or its shape by modifying the system (emitter–receiver couples) directivity patterns. The latter was here simply altered by adjusting the emitter radius size. The volume sampled by one receiver possesses a complex 3D shape, defined by the intersection of the isotravel lines of the pulse contouring the measurement gate (region in space where the time necessary for a pulse to travel from the emitter to the receiver remains constant) within the mainlobe of the directivity patterns of the emitter–receiver couple. In the present case, as the emitter radius is increased (decreased), the mainlobe of the emitter–receiver directivity patterns narrows (widens). Alternatively, increasing the pulse length leads to a vertical expansion of the sampled volume and conserves the aspect ratio. These regimes are not necessarily practicable configurations but they permit the study of the effect of measurement collocation on velocity and concentration. The collocation of the volumes insonified by each receiver is an important parameter when turbulence-resolved

multi-component velocity estimations are of concern. Figure 8 illustrates the position of the particles insonified in one measurement gate ($d_k = 107.9$ mm) by a 2 μs–duration pulse to be recorded by each of the two receivers R_1 and R_2 (Fig. 4). The final echo recorded by each receiver is the sum of the backscatter from each individual particle within the volume weighted by the directivity patterns of each bistatic emitter–receiver couple.

As the emitter radius changes, the resulting sampled volume is stretched both horizontally (y direction) and vertically (z direction). For the smaller emitter radii, the regions in space seen by both receivers begin to differ substantially, leading to increasingly more non-colocalized measurements as a systematic measurement position error in the geometric multi-component velocity reconstruction [Eq. (12)], which assumes a theoretical volume center on the emitter axis [blue cross in Figs. 8(a), 8(c), and 8(e)]. In these calculations, the measurement position is set at the sampled volume centroid, computed as the barycenter of the directivity beam patterns across the isotravel lines defining the gate of interest.

Furthermore, measurement resolution is also decreased due to the increasing vertical extents of the sampled volumes. Moreover, as the emitter radius decreases, the vertical distribution of the insonified particles contributing to the echo becomes increasingly less homogeneous due to the narrow upper tail of the sampled volume, with less targets located near the thin upper tail of the sampled volume [visible on Figs. 8(d) and 8(f) in the xz plane). Consequently, targets located in the narrowing upper tail contribute to a lesser
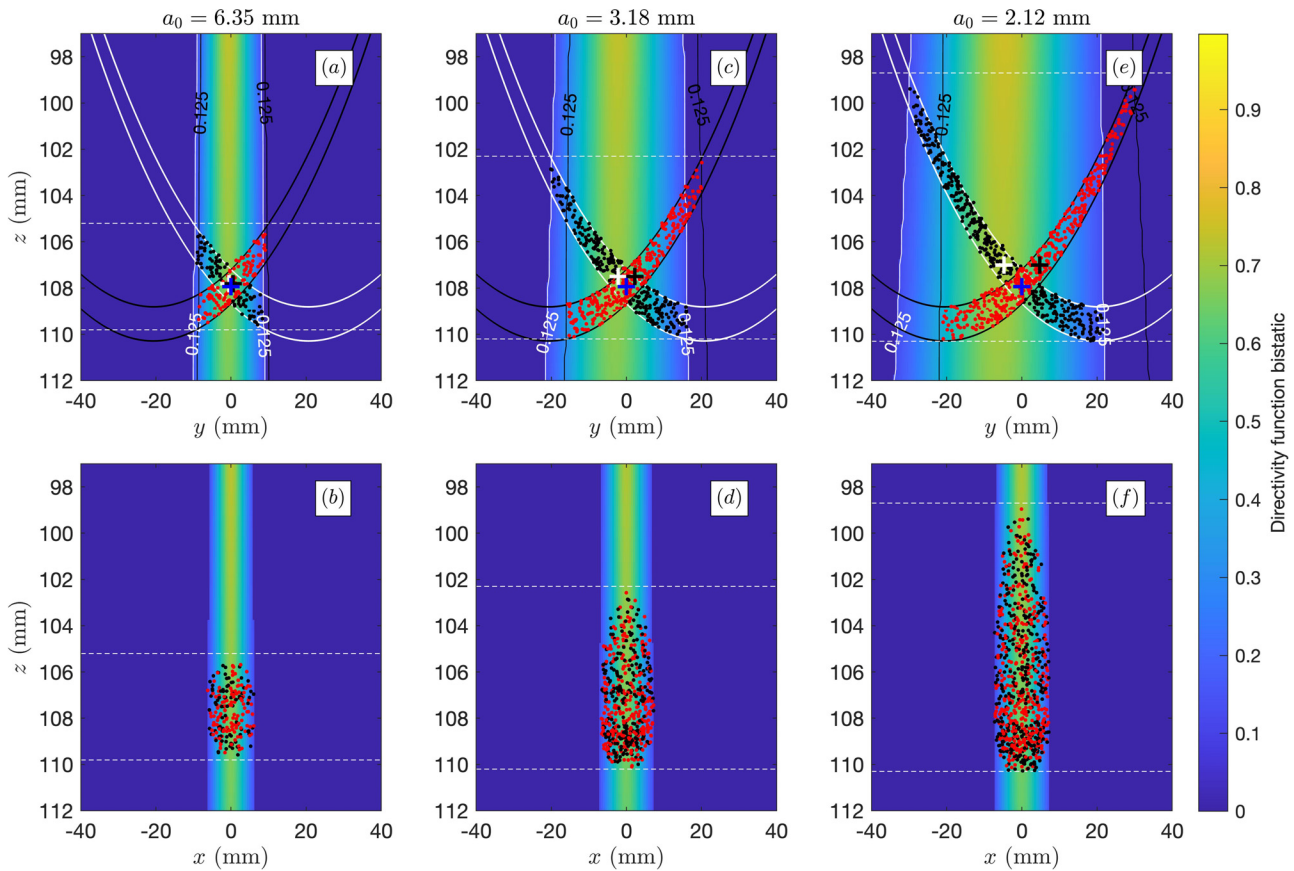
J. Acoust. Soc. Am. 155 (4), April 2024

Fromant et al. 2827

FIG. 8. (Color online) Representation of the volumes sampled in (a)(c)(e) the y-z plan and (b)(d)(f) the xz plane by each receiver R_1 and R_2 in bistatic configurations used in (a) and (b) run 1, (c) and (d) 13, and (e) and (f) 15. Black (red) dots represent the position of particles (projected on the plane of interest) contributing to the backscattered echo within the volume sampled by the right (left) receiver R_1 (R_2) for the current pulse. Panels (a)–(c) show the theoretical volume center (blue +) used for velocity reconstruction [Eq. (12)], and the volume centroids relative to the E-R_1 (white +) and E-R_2 (black +) transducers couples. The colormap reveals the mainlobe of the directivity patterns for the emitter and R_1 receiver E-R_1 transducer couple for $D_{R1}^2 > 0.125$ (or $10 log_{10} D_{R1}^2 > -9$ dB). The value 0.125 has been chosen here for illustration purpose as it encompasses most of the system directivity function mainlobe on the figure (no threshold is used in the calculations). The vertical extent of the sampled volume is indicated with dashed white lines and is common for both emitter–receiver couples as the system is axisymmetric around the emitter axis.

number of consecutive pulses than those located in the lower part. Due to the complex 3D shape of the sampled volume, this effect persists when increasing the pulse length by a few cycles (not shown here for brevity). Finally, Figs. 8(a) and 8(b) confirms the co-located feature of the standard ACVP system geometry in Hurther *et al.* (2011) corresponding to Runs 1–5 with $a_0 = 6.35$ mm.

The previous effects associated with different sampled volume settings (pulse time-length and emitter radius) are visible in the simulated statistical distributions of particle velocity. Figures 9 and 10 present the instantaneous velocities distribution [Eq. (12)] estimated using two consecutive pulses for the case of varying pulse length (Table I, Runs 1 and 6–9) and emitter radius (Table I, Runs 1 and 10–15), respectively, for a fixed particle advection velocity of 0.5 m/s.

Increasing the pulse length appears to have no impact on the estimated velocity distribution [Figs. 9(a)–9(e)] nor on the normalized autocorrelation function in terms of mean correlation time scale [Fig. 9(f)]. In the present case of unidirectional constant flow conditions with particle velocities in y-direction, the increase in the sampled volume in

z-direction does not increase the characteristic correlation time; this is in accordance with the previous hypothesis relating correlation of consecutive pulses to particle residence time within the sampled volume.

Changing the sampled volume aspect ratio by decreasing a_0 seems, however, to impact the velocity distributions. As the mainlobe of the directivity patterns widens (decreasing emitter radii), the width of the distribution is controlled by the parameter $\alpha = \sqrt{1 - \rho(t_{PRF})^2}$; this appears to increase for $a_0 = 4.23$ mm and below [Figs. 10(e)–10(g)], as a probable result of a higher geometric velocity reconstruction error of the horizontal velocity [see Figs. 8(c) and 8(e)]. Consecutive pulses are also seen to reduce coherence more rapidly as a_0 decreases [Fig. 10(h)]. The extent of this loss of coherence is however less sensitive here compared to varying advection speed [Fig. 6(f)] and may be the result of the inhomogeneous vertical distribution of the particles contributing to the echo as the system directivity patterns stretches horizontally [Figs. 8(d) and 8(f)]. It is also noted that a slight decrease in $\rho(t_{PRF})$ (increase in α) is also observed for the smaller sampled volume [Fig. 10(a)],
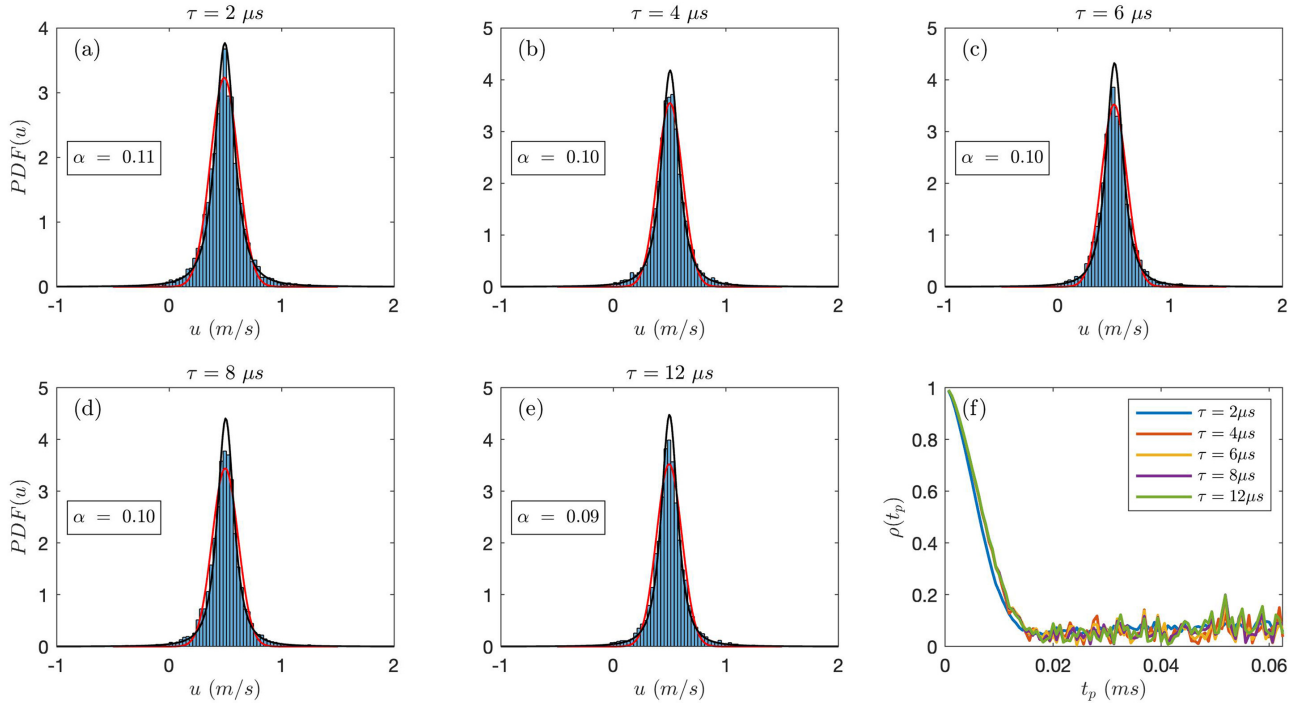
FIG. 9. (Color online) (a)–(e) PDF(v) of the instantaneous velocities (using two consecutive pulses) for various sampled volumes controlled by the pulse length τ (Runs 1 and 6–9) and fixed advection velocity, $v = 0.5$ m/s. The red lines are Normal fits to the distributions, the black lines are Pearson type VII fits to the distribution. (f) Normalized autocorrelation function of the estimated velocity time series for all pulse length cases.

as the residence time of the particles traversing the volume is decreased: the smaller sampled volumes [$\mathcal{O}(10\,\text{mm}^3)$; see Table I] do not ensure permanent presence of particles within the –3 dB volume, and the question of the minimum sampled volume size for a given particle volume concentration arises leading to a potential discontinuity in the measured time-resolved particle concentration.

Time series of backscattered amplitudes for varying pulse length (Fig. 11) and emitter radii (Fig. 12) at a constant particle advection speed of 0.5 m/s are Rayleigh distributed as
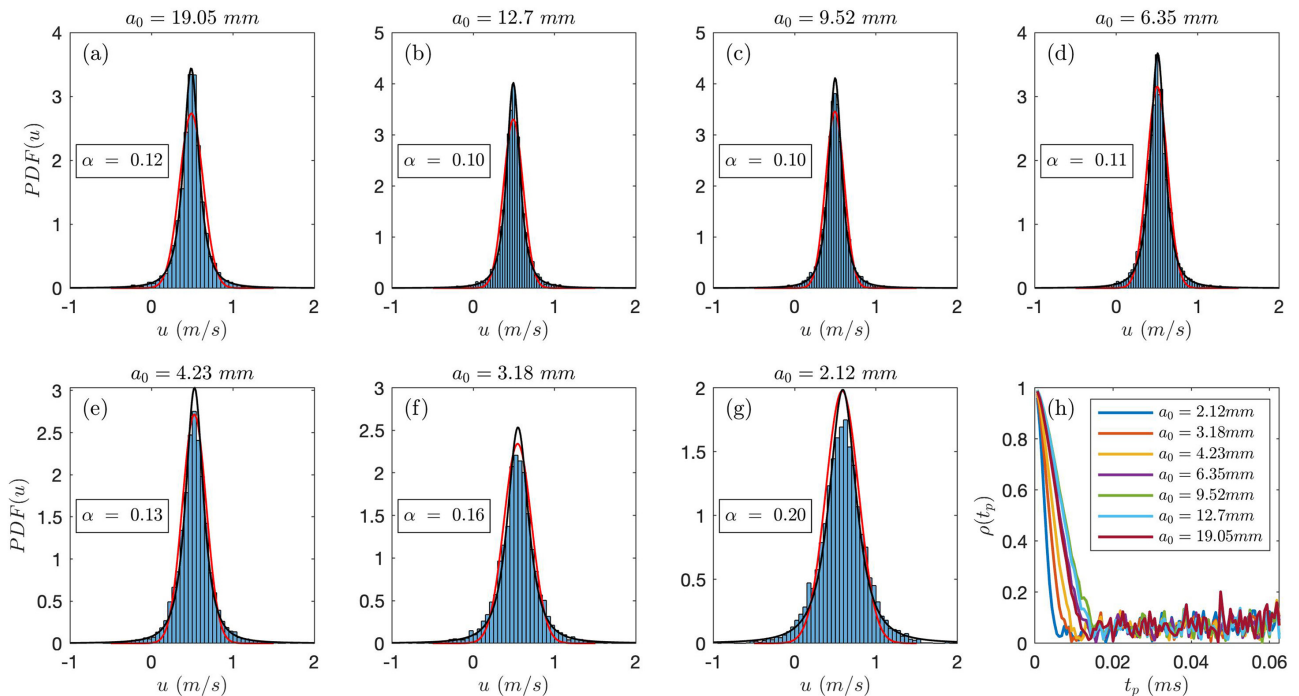
FIG. 10. (Color online) (a)–(g) PDF(v) of the instantaneous velocities (using two pulses) for various sampled volume controlled by the emitter radius (Runs 1 and 10–15) and fixed advection velocity, $v = 0.5$ m/s. The red lines are Normal fits to the distributions, the black lines are Pearson type VII fits to the distribution. (h) Normalized autocorrelation function of the estimated velocity time series for all sampled volume cases.

J. Acoust. Soc. Am. **155** (4), April 2024

Fromant *et al.* 2829

FIG. 11. (Color online) (a)–(e) PDF (S_a) of the backscattered amplitudes for sampled volume ranging from $108\,\text{mm}^3$ ($\tau = 2\,\mu s$) to $650\,\text{m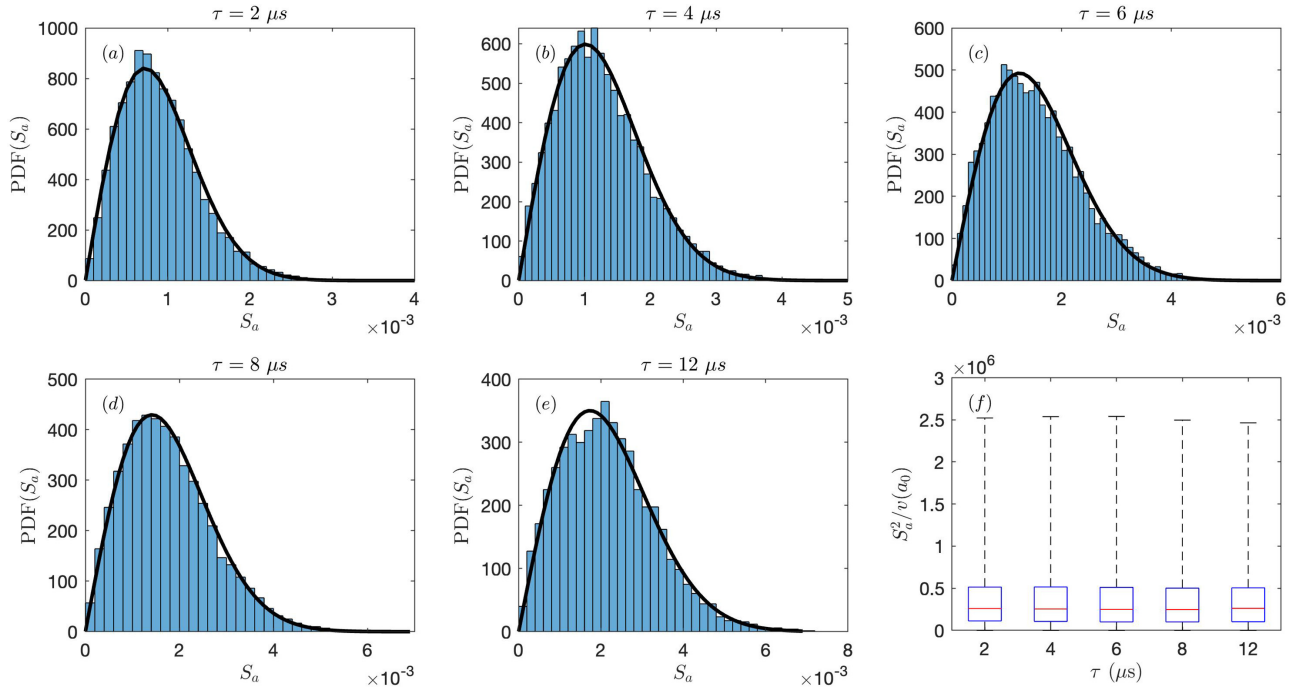m}^3$ ($\tau = 12\,\mu s$) (Runs 1 and 6–9). The sampled volumes were adjusted by tuning the pulse length τ. The black lines are Rayleigh fits to the distributions. (f) Boxplots representation of the volume-normalized mean squared backscatter distributions for all sampled volumes where the red lines represent the median value, and the extrema of the dotted lines show the extrema of the distribution. The upper and lower levels of the boxes in the boxplot refer to the 25th and 75th percentiles.
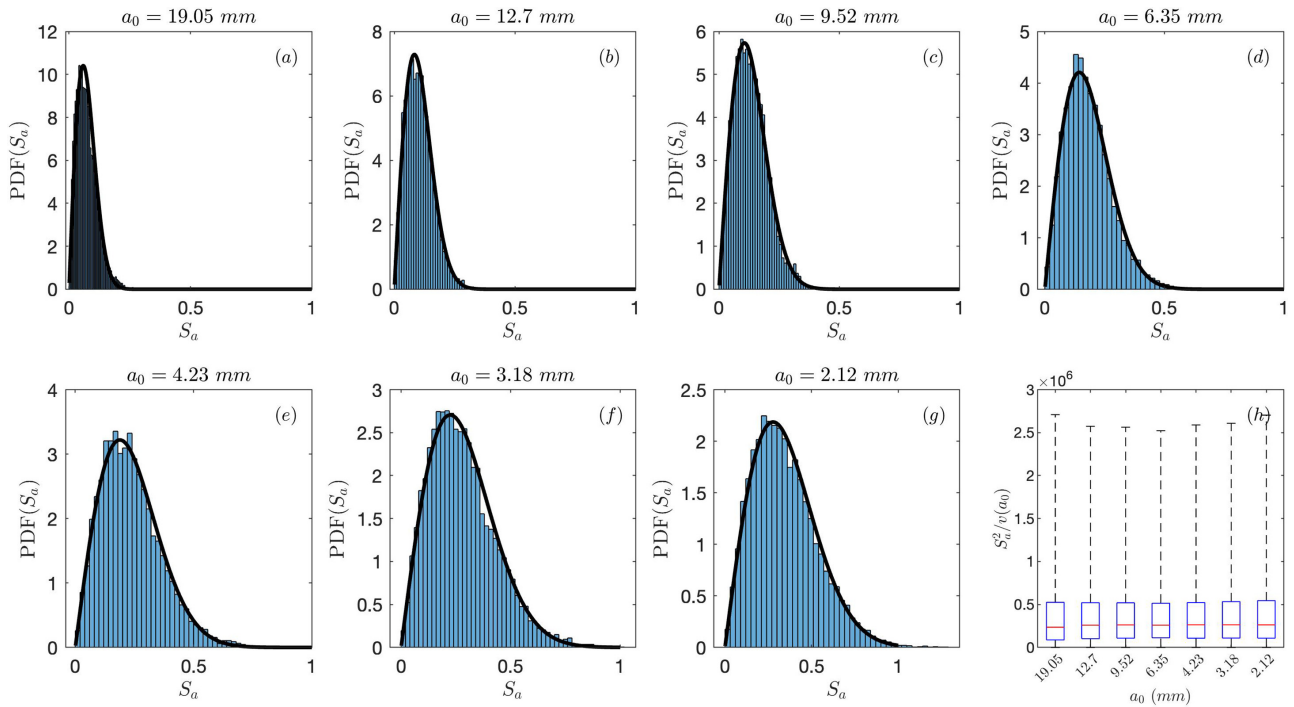
FIG. 12. (Color online) (a)–(g) PDF (S_a) of the backscattered amplitudes for sampled volume ranging from $17\,\text{mm}^3$ ($a_0 = 19\,\text{mm}$) to $385\,\text{mm}^3$ ($a_0 = 2.1\,\text{mm}$) (Runs 1 and 10–15). The sampled volumes were adjusted by adjusting the emitter radius a_0. The black lines are Rayleigh fits to the distributions. (h) Boxplots representation of the volume-normalized mean squared backscatter distributions for all sampled volumes where the red lines represent the median value, and the extrema of the dotted lines show the extrema of the distribution. The upper and lower levels of the boxes in the boxplot refer to the 25th and 75th percentiles.

2830   J. Acoust. Soc. Am. **155** (4), April 2024

Fromant *et al.*

expected, displaying similar mean square values once normalized by the sampled volumes $v_0(a_0)$. The widths of the distributions are fairly similar to the case of varying velocities, as shown in Fig. 7(f). No particular effect on the normalized mean squared backscattered amplitudes can be seen in the present case of unidirectional constant flow simulation due to volume changes [Fig. 11(f) and Fig. 12(h)].

As shown in the present case of unidirectional constant flow simulations, the model offers opportunities to investigate the role of the sampled volume in the final velocity estimate. It particularly highlights the importance of ultrasound beam pattern associated with sensor geometry for velocity measurements. When high-resolution multi-component velocity measurements are aimed at a given small flow scale (driven by viscosity or by flow turbulence), the different bistatic radial velocity components must be measured simultaneously (at turbulence-driven scale) at the same position and within a sampled volume of size being larger than the flow scale to be resolved. In typical highly turbulent flow conditions, Lemmin and Rolland (1997), Shen and Lemmin (1999), and Hurther et al. (2011) designed a bistatic system using wide angle receivers with beam patterns overlapping a wide domain of the highly directive emitter beam patterns (see Fig. 4). This allowed collocated measurements [Fig. 8(a)] at a distance far from the sensor induced flow disturbance region (typically of a few centimeters below sensors) with a vertical resolution converging asymptotically with range, towards the monostatic resolution of $c\tau/2$. Hay et al. (2012a) and Hay et al. (2012b) selected a bistatic system composed of identical high-directivity transducers for both emission and reception, thus constraining the region of collocated velocity measurements around the point of intersection of the emitter and receiver beam patterns (Zedel et al., 2021) but sampling the vertical domain with a constant spatial resolution of $c\tau/2$.

Both these systems have demonstrated their potential to profile sediment fluxes in highly turbulent sediment-laden flows (Smyth et al., 2002; Hurther and Lemmin, 2003; Fromant et al., 2018; Fromant et al., 2019; Zedel et al., 2021), and while in this study the choice has been directed towards modelling ACVP systems, the present approach can be transposed to other geometries. With consistent velocity and backscatter amplitude statistics returned, the present point-particle approach can thus be regarded as a simulation tool adapted to the examination of hydroacoustic particle flux measurements with the capability to investigate the system related effects of beam pattern geometry and effects due to flow conditions.

V. MEASUREMENT ACCURACY OF SEDIMENT FLUX

Hydroacoustic profilers, such as the acoustic particle flux profiler (APFP) (Shen and Lemmin, 1997), acoustic concentration and velocity profiler (ACVP) (Hurther et al., 2011), or multi-frequency coherent Doppler profiler (MFDop) (Hay et al., 2012a,b) systems provide time-resolved measurements of sediment fluxes at rates resolving

the smallest flow scale involved in sediment transport. For the wide majority of sediment-laden flow conditions, this typically implies turbulent microscales on the order of 0.01 s for the velocity and 0.1 s for the smallest concentration scales (Thorne and Hurther, 2014). As a consequence, sediment fluxes defined as the local product of sediment velocity and concentration need to be measured at rates of about 10 Hz. Resolving these time scales is linked to our capability to observe the flow properties (velocity, concentration) quasi-instantaneously, at a temporal rate sufficiently high to ensure signal coherency, necessary for the flow accuracy, over a period of time sufficiently large to reach incoherent scattering conditions for the concentration estimate. For velocity measurements, pulse-to-pulse phase coherency over received consecutive echoes is guaranteed when the pulse repetition period is much smaller (usually set to ten times) than the correlation time scales of the Doppler signal discussed in Sec. IV A (Figs. 9 and 10). This implies typical PRF values on the order of 1 KHz. On the other hand, for particle concentration measurements, in order to suppress the contribution of the coherent phase term in Eq. (7a) (second term in the parenthesis), averaging of the echo amplitudes S_a must be done over sufficient statistical independent pulse echoes so that the coherent phase term becomes a random variable with a zero valued average. The number of independent realizations for the calculation of one concentration estimate determines the statistical bias errors on the time-resolved concentration measurement as discussed by Thorne and Hurther (2014). However, in Thorne and Hurther (2014), no explanation considering sampled volume geometry and flow conditions effects was given to justify the number of statistically independent pulse echoes needed for a robust (i.e., *weakly* statistically biased) time-resolved particle concentration estimate.

When it comes to time-resolved flux measurement, no clear consensus exists on how many consecutive pulses are then necessary to build a robust time-resolved estimate of the concentration when backscattered echoes are only partially decorrelated, and the question relative to the convergence of such partially incoherent observations arises. For this purpose, estimation of the measurement accuracy of time-resolved sediment velocity, concentration, and flux is investigated here considering the random scattering process (at the scale of the sampled volume) discussed above (Sec. IV A) under imposed constant particle speed (as a proxy of unidirectional constant sediment-laden flow conditions). Estimating the measurement accuracy under these simplified flow conditions is a crucial first step before considering more complex and realistic flow conditions involving turbulence induced random fluctuations of velocity, concentration, and sediment flux.

Three 50 s long runs (Runs 16–18 using the settings of Runs 1, 3, and 4, respectively; Table I) were generated for the estimation of the measurement accuracy of time-resolved velocity, concentration, and sediment flux. The sensor geometry and pulse time-length settings for these runs correspond to standard ACVP configuration.

J. Acoust. Soc. Am. **155** (4), April 2024

10 June 2024 17:00:44

Fromant *et al.* 2831

These runs were split into 50 sub-runs of 1 s each. For each sub-run, velocity v [Eqs. (10)–12)], concentration M [Eqs. (15)–(17)], and flux Mv were calculated using a growing sequence of m consecutive pulses, from $m = 2$ to 1600 for time-resolved estimation. Therefore, because $f_{PRF} = 1600$ Hz, the lowest and highest simulated time-resolutions are 1 s and 1.25×10^{-3} s. These time-resolution values are called integration time in the following because they represent the time interval t over which the consecutive echoes are averaged for one estimate using the pulse-pair technique. In this way, time-resolved estimates of v and M could be produced (albeit the time-resolved feature becomes questionable for high values of m) over a range of temporal rate varying from 1 to 800 Hz. Thus, each sub-run produced a realization of how v, M and Mv converged over 1 s. Figures 13(a)–13(c) envelopes displays the evolution as a function of integration time of the standard deviation (over 50, sub-run, realizations) of estimates v [Fig. 13(a)],

M [Fig. 13(b)], and Mv [Fig. 13(c)] for particles moving at 0.1, 0.5, and 0.75 m/s. For each quantity in Figs. 13(a)–13(c), a reference mean value (represented as the thick colored solid curve) is calculated from an average over the particles present within the sampled volume, the number of which can vary slightly from one pulse to another due to exiting and entering particles. Note, for instance, the residual mean value fluctuations seen in the reference mean concentration and sediment flux values shown by the slightly oscillating colored solid curves [Figs. 13(b) and 13(c)]. The magnitude of these small oscillations represents the minimum achievable measurement error since its origin is associated with a sampled volume size close to the minimal size for a representative (spatially averaged) volume particle concentration. For larger sampled volumes, this residual oscillation vanishes to zero; however, the aim here is to examine the local small-scale mass concentrations. The optimal sample volume size for the simulated (low) particle
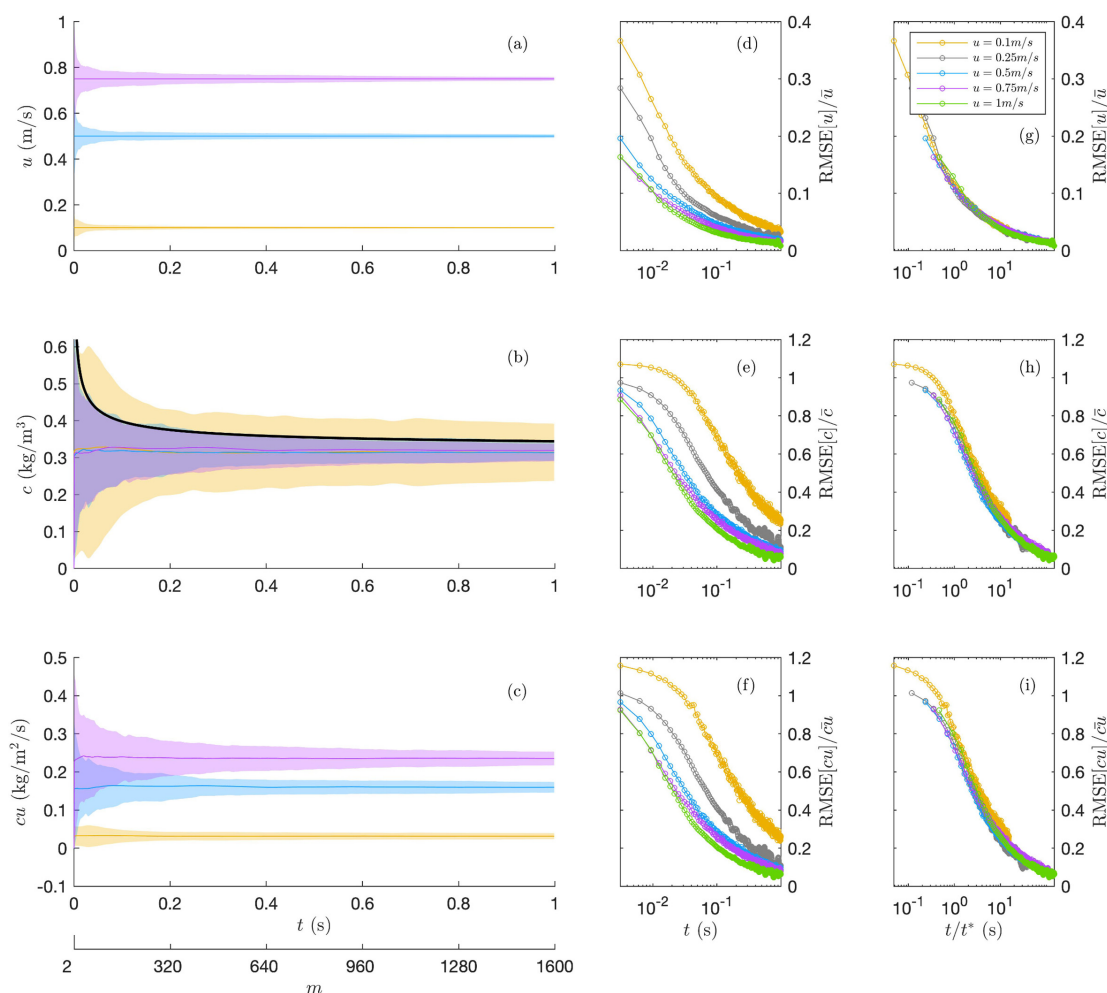

FIG. 13. (Color online) Evolution of the standard deviation envelope of the (a) time-resolved velocity, (b) concentration, (c) flux estimates (color patches) with respect to the integration time (which is linked to the number of consecutive samples necessary to create an estimate), for advection velocities of 0.1 m/s (yellow, Run 16), 0.5 m/s (blue, Run 17), and 0.75 m/s (magenta, Run 18). The standard deviations were derived from 50 independent 1 s duration samples. In panels (a)–(c), the solid-colored lines correspond to the mean expected value based on the actual particle number within the sampled volume. On panels (b), the thick black line shows the $1/\sqrt{m}$ behavior. The evolution of the normalized root mean squared errors with respect to integration time are also represented for (d) velocity, (e) concentration, (f) flux (Runs 1–5). Panels (g)–(i) represent the same data as panels (d)–(f), with the x axis normalized by the decorrelation time t^*.

2832   J. Acoust. Soc. Am. **155** (4), April 2024

Fromant *et al.*

volume concentration condition can be found by determining the minimal size above which the oscillation of the reference mean concentration value remains below a fixed relative error value. In the present case, Figs. 13(b) and 13(c) show that this minimal error is below a few percent which ensures the appropriateness of the tested sampled volume size.

For each particle advection velocity case, the estimated quantities display high uncertainty for small numbers of consecutive pulses m (or small integration time t). The velocity bias error [Fig. 13(a)] collapses at a faster rate than the concentration error [Fig. 13(b)]. Only a few consecutive pulses are required for the pulse-pair method to remove the noise due to the spatial distribution of the particles within the sampled volume. Also, it can be visually inferred on Fig. 13(a) that the error on velocity decreases faster for lower particle advection speeds, whereas the opposite trend can be observed for the concentration error where the error magnitude remains high for the 0.1 m/s case [Fig. 13(b)]. This supports the idea that longer particle residence time within the sampled volume maintains phase coherence over more consecutive pulses [Fig. 6(f)] as a source of statistical bias errors in the concentration estimation.

For all velocity cases, the black solid curve in Fig. 13(b) shows that the concentration bias errors display a trend in $1/\sqrt{m}$ where m is the number of independent echo amplitude realizations. This trend confirms the Rayleigh distributed echo amplitudes as shown in Thorne and Hurther (2014) when incoherent scattering conditions are met. Furthermore, it can be seen that for the smaller, $0.1 \, \mathrm{ms}^{-1}$, velocity case, the bias error becomes larger and that the range with the trend in $1/\sqrt{m}$ is shifted towards larger integration time values. This supports that longer particle residence time within the sampled volume maintains coherence over more consecutive pulses [Fig. 6(f)] as a source of random errors in the concentration estimation.

These different scales of convergence for the velocity and concentration estimates are highlighted on Figs. 13(d) and 13(e), respectively, representing the evolution of the normalized root mean squared error (rmse), as a function of integration time. An order of magnitude separates the normalized rmse for velocity [$\mathcal{O}(10^{-2} - 10^{-1})$] and concentration [$\mathcal{O}(10^{-1} - 10^{0})$]. For both estimates, the magnitude of the rmse decreases, according to both increasing advection speed and integration time. As anticipated from Fig. 13(b), the normalized rmse for the concentration exhibits a slow decrease rate with respect to integration time for small integration times, for which the estimate has not yet met the criterion of incoherent scattering. This trend is more pronounced as the particle advection velocity is reduced as previously observed from Fig. 13(b).

The order of magnitude of convergence rate existing between velocity and concentration estimates has a critical impact on the bias error of sediment flux [Fig. 13(c)], which follows the trend of the concentration error [Fig. 13(f)]. Although this is not a problem for time-averaged (usually called net) flux estimations, especially in unidirectional

constant flow conditions, this suggests that getting (weakly biased) time-resolved sediment flux measurements depends first on the measurement accuracy of time-resolved concentration. This is in good agreement with the typical ratio of 1 order of magnitude between the time-resolutions of pulse-coherent velocity and concentration (and sediment flux) measurements obtained with the ACVP technology (Naqshband *et al.*, 2014; Revil-Baudard *et al.*, 2015, Fromant *et al.*, 2018; Grossmann *et al.*, 2023). How turbulent flow scales smaller than the sampled volume size affect coherence time scale of the Doppler signal and velocity and concentration statistics has not been studied in great detail so far. The present numerical point-particle model tool offers this type of investigation, where an adapted description of the scattering from turbulent microstructures to account for the temporal fluctuation of the scattered field due to the time-varying random medium (Ishimaru, 1978; Shen and Lemmin, 1997) and subsequent Doppler frequency spread anticipated in the temporal frequency spectrum of the return echos could be implemented.

Finally, the integration time in the plots of normalized rmse plots was made dimensionless with respect to the correlation time scale t^* for each simulated case. t^* is determined as the time separating two pulses beyond which the normalized autocorrelation function drops below a value of 0.1 [Fig. 6(f)] [$\rho(t^*) = 0.1$]. This decorrelation time increases with decreasing particle advection speed, as shown on [Fig. 6(f)]. The final curves of normalized rmse of v [Fig. 13(g)], M [Fig. 13(h)], and Mv [Fig. 13(i)] appear to collapse after $t/t^* = 1$ towards a common curve, supporting the supposition that the mean particle residence time within the sampled volume is the governing parameter of the measurement error in sediment flux estimations. Subsequently, beyond $t/t^* = 1$, the incoherence criterion begins to be met as the estimate is assembled from consecutive independent echo amplitude realizations. Thus, as the integration time is extended, the evaluation of the velocity is improved with the pulse-pair method, as the noise in the estimate of the phase of the autocorrelation function is filtered out. Further, the value computed for concentration becomes more accurate due to the incoherence averaging criterion being met. For integration time above $100 \, t^*$, the normalized rmse for the concentration and flux is 8% of the mean value. Interestingly, this value is close to the 10% normalized error mass that would be expected for a Rayleigh distribution (Thorne and Hurther, 2014).

VI. SUMMARY AND CONCLUSIONS

A new numerical model capable of simulating the ultrasound scattered echoes of an insonified particle cloud moving with unidirectional constant flow speed using a point-particle scattering approach has been described and validated. The model considers each individual particle in a 3D domain surrounding the volumes sampled by a bistatic sonar system with controlled geometry. The model considers transducers' beam patterns, spherical spreading, sound

J. Acoust. Soc. Am. **155** (4), April 2024

Fromant *et al.*   2833

absorption, and scattering properties, as well as flow properties. Accurate control of the sampled volume shape and position can be achieved by manipulating the transducers' dimensions and geometry. The present model differentiates itself from previous numerical models (Zedel, 2008; Zedel *et al.*, 2021) by considering the scattering characteristics of individual sediment scatterers and by allowing an examination of the cloud effects on the measured velocity and sediment concentration profiles for sediment flux profile estimates.

The model performance was evaluated in dilute flow conditions, without particle scattering induced attenuation effects, as an initial step before considering more realistic and complex sediment-laden flows in highly turbulent flows. Under these conditions, the model returns consistent estimates of velocity and backscattered amplitudes for varying particle advection speeds and sampled volume size and shape, revealing the importance of measurement collocation in multi-bistatic system configuration for multi-component velocity estimation. An examination of the temporal autocorrelation function of the Doppler signal also supports the hypothesis of consecutive pulses remaining correlated as long as the same particle cloud is insonified within the sampled volume over the number of consecutive pulses used for a time-resolved measurement.

Application to the estimation of the measurement accuracy of sediment flux in steady unidirectional flow conditions (with no turbulent motion) is also considered. The dichotomy of requiring coherent measurements for the flow accuracy, and independent, incoherent measurements for concentration is demonstrated by the difference in convergence time scales of both velocity and concentration estimates. This difference is at the origin of the bias error in time-resolved sediment flux estimations, which is shown to be dominated by the statistical bias error in the concentration estimate. The final error in the flux is seen to be partially controlled by the residence time of particles within the sampled volume, also known as the transit time effect in hydroacoustic turbulence measurements studied by Lhermitte and Lemmin (1990).

Finally, the present numerical model offers interesting investigation performances for understanding the leading scattering processes in hydroacoustic sediment flux measurements. The model's design makes it a supporting tool adapted to investigate novel techniques for more robust flux estimation and further highlight measurement uncertainties. These uncertainties fundamentally affect:

(1) the measurements' temporal accuracy, due to the interplay existing between coherent and incoherent requirements for velocity and concentration estimations, respectively,
(2) the measurements' spatial accuracy, due to the necessity of collocated measurements in bistatic configuration.

The present model can further be utilized to assess a number of different system configurations (implemented in widely used UVP, ADVP systems) and flow scenarios considering more realistic flow regimes representative of coastal and fluvial sediment-laden flows.

AUTHOR DECLARATIONS
Conflict of Interest

The authors have no conflicts to disclose.

DATA AVAILABILITY

The data that support the findings of this study are available from the corresponding author upon reasonable request.

Atkinson, P., and Wells, P. N. T. (**1977**). "Pulse-Doppler ultrasound and its clinical application," Yale J. Biol. Med. **50**(4), 367–373, available at https://www.ncbi.nlm.nih.gov/pmc/articles/pmid/143803/.

Bamler, R., and Hartl, P. (**1998**). "Synthetic aperture radar interferometry," Inverse Probl. **14**(4), R1.

Capart, H., and Fraccarollo, L. (**2011**). "Transport layer structure in intense bed-load," Geophys. Res. Lett. **38**(20), L20402, https://doi.org/10.1029/2011GL049408.

Chauchat, J., Hurther, D., Revil-Baudard, T., Cheng, Z., and Hsu, T.-J. (**2022**). "Controversial turbulent Schmidt number value in particle-laden boundary layer flows," Phys. Rev. Fluids **7**(1), 014307.

Cheng, Z., Chauchat, J., Hsu, T. J., and Calantoni, J. (**2018**). "Eddy interaction model for turbulent suspension in Reynolds-averaged Euler–Lagrange simulations of steady sheet flow," Adv. Water Resour. **111**, 435–451.

Dillon, J., Zedel, L., and Hay, A. E. (**2011**). "Asymptotic properties of an autocorrelation coefficient for coherent Doppler sonar," J. Atmos. Ocean. Technol. **28**(7), 966–973.

Dillon, J., Zedel, L., and Hay, A. E. (**2012a**). "Simultaneous velocity ambiguity resolution and noise suppression for multifrequency coherent Doppler sonar," J. Atmos. Ocean. Technol. **29**(3), 450–463.

Dillon, J., Zedel, L., and Hay, A. E. (**2012b**). "On the distribution of velocity measurements from pulse-to-pulse coherent Doppler sonar," IEEE J. Ocean. Eng. **37**(4), 613–625.

Fromant, G., Mieras, R. S., Revil-Baudard, T., Puleo, J. A., Hurther, D., and Chauchat, J. (**2018**). "On bedload and suspended load measurement performances in sheet flows using acoustic and conductivity profilers," J. Geophys. Res. Earth Surf. **123**(10), 2546–2562.

Fromant, G., Hurther, D., Cáceres, I., and Ribberink, J. S. (**2019**). "Wave boundary layer hydrodynamics and sheet flow properties under large-scale plunging-type breaking waves," J. Geophys. Res. Oceans **124**(1), 75–98.

Garbini, J. L., Jorgensen, J. E., Garbini, J. L., Forster, F. K., and Jorgensen, J. E. (**1982**). "Measurement of fluid turbulence based on pulsed ultrasound techniques. Part 1. Analysis," J. Fluid Mech. **118**, 471–505.

Grossmann, F., Hurther, D., van Der Zanden, J., Cáceres, I., Sánchez-Arcilla, A., and Alsina, J. M. (**2022**). "Near-bed sediment transport during offshore bar migration in large-scale experiments," J. Geophys. Res.: Oceans **127**(5), e2021JC017756, http://dx.doi.org/10.1029/2021JC017756.

Grossmann, F., Hurther, D., van der Zanden, J., Sánchez-Arcilla, A., and Alsina, J. M. (**2023**). "Near-bed sediment transport processes during onshore bar migration in large-scale experiments: Comparison with offshore bar migration," J. Geophys. Res.: Oceans **128**(3), e2022JC018998, http://dx.doi.org/10.1029/2022JC018998.

2834   J. Acoust. Soc. Am. **155** (4), April 2024

Fromant *et al.*

Guta, H., Hurther, D., and Chauchat, J. (**2022**). "Bedload and concentration effects on turbulent suspension properties in heavy particle sheet flows," J. Hydraul. Eng. **148**(7), 04022012.

Hay, A. E., Zedel, L., Cheel, R., and Dillon, J. (**2012a**). "Observations of the vertical structure of turbulent oscillatory boundary layers above fixed roughness beds using a prototype wideband coherent Doppler profiler: 1. The oscillatory component of the flow," J. Geophys. Res.: Oceans **117**(C3), C03005, https://doi.org/10.1029/2011JC007113.

Hay, A. E., Zedel, L., Cheel, R., and Dillon, J. (**2012b**). "Observations of the vertical structure of turbulent oscillatory boundary layers above fixed roughness using a prototype wideband coherent Doppler profiler: 2. Turbulence and stress," J. Geophys. Res.: Oceans **117**(C3), C03006, https://doi.org/10.1029/2011JC007114.

Hurther, D., and Lemmin, U. (**2001a**). "A correction method for turbulence measurements with a 3D acoustic Doppler velocity profiler," J. Atmos. Ocean. Technol. **18**(3), 446–458.

Hurther, D., and Lemmin, U. (**2001b**). "Shear stress statistics and wall similarity analysis in turbulent boundary layers using a high-resolution 3-D ADVP," IEEE J. Ocean. Eng. **25**, 446–457.

Hurther, D., and Lemmin, U. (**2003**). "Turbulent particle flux and momentum flux statistics in suspension flow," Water Resour. Res. **39**(5), 1139, https://doi.org/10.1029/2001WR001113.

Hurther, D., and Thorne, P. D. (**2011**). "Suspension and near-bed load sediment transport processes above a migrating, sand-rippled bed under shoaling waves," J. Geophys. Res.: Oceans **116**(C7), C07001, https://doi.org/10.1029/2010JC006774.

Hurther, D., Thorne, P. D., Bricault, M., Lemmin, U., and Barnoud, J.-M. (**2011**). "A multi-frequency acoustic concentration and velocity profiler (ACVP) for boundary layer measurements of fine-scale flow and sediment transport processes," Coast. Eng. **58**(7), 594–605.

Ishimaru, A. (**1978**). *Wave Propagation and Scattering in Random Media* (Academic Press, New York), Vol. 2, pp. 329–375.

Lemmin, U., and Rolland, T. (**1997**). "Acoustic velocity profiler for laboratory and field studies," J. Hydraul. Eng. **123**(12), 1089–1098.

Lhermitte, R., and Lemmin, U. (**1990**). "Probing water turbulence by high frequency Doppler sonar," Geophys. Res. Lett. **17**(10), 1549–1552.

Lhermitte, R., and Lemmin, U. (**1994**). "Open-channel flow and turbulence measurement by high-resolution Doppler sonar," J. Atmos. Ocean. Technol. **11**(5), 1295–1308.

Lhermitte, R., and Serafin, R. (**1984**). "Pulse-to-pulse coherent Doppler sonar signal processing techniques," J. Atmos. Ocean. Technol. **1**(4), 293–308.

Mo, L. Y. L., and Cobbold, R. S. C. (**1992**). "A unified approach to modeling the backscattered Doppler ultrasound from blood," IEEE Trans. Biomed. Eng. **39**(5), 450–461.

Moore, S. A., and Hay, A. E. (**2009**). "Angular scattering of sound from solid particles in turbulent suspension," J. Acoust. Soc. Am. **126**(3), 1046–1056.

Naqshband, S., Hoitink, A. J. F., McElroy, B., Hurther, D., and Hulscher, S. J. (**2017**). "A sharp view on river dune transition to upper stage plane bed," Geophys. Res. Lett **44**(22), 11437–11444, http://dx.doi.org/10.1002/2017GL075906.

Naqshband, S., Hurther, D., Giri, S., Bradley, R. W., Kostaschuk, R. A., Venditti, J. G., and Hoitink, A. J. F. (**2021**). "The influence of slipface angle on fluvial dune growth," J. Geophys. Res. Earth Surf. **126**(4), e2020JF005959, https://doi.org/10.1029/2020JF005959.

Naqshband, S., Ribberink, J. S., Hurther, D., and Hulscher, S. (**2014**). "Bed load and suspended load contributions to migrating sand dunes in equilibrium," J. Geophys. Res. Earth Surf. **119**(5), 1043–1063.

Pepe, A., and Calò, F. (**2017**). "A review of interferometric synthetic aperture RADAR (InSAR) multi-track approaches for the retrieval of Earth's surface displacements," Appl. Sci. **7**(12), 1264.

Pugh, F. J., and Wilson, K. C. (**1999**). "Velocity and concentration distributions in sheet flow above plane beds," J. Hydraul. Eng. **125**(2), 117–125.

Revil-Baudard, T., Chauchat, J., Hurther, D., and Barraud, P.-A. (**2015**). "Investigation of sheet-flow processes based on novel acoustic high-resolution velocity and concentration measurements," J. Fluid Mech. **767**, 1–30.

Revil-Baudard, T., Chauchat, J., Hurther, D., and Eiff, O. (**2016**). "Turbulence modifications induced by the bed mobility in intense sediment-laden flows," J. Fluid Mech. **808**, 469–484.

Shen, C., and Lemmin, U. (**1997**). "Ultrasonic scattering in highly turbulent clear water flow," Ultrasonics **35**(1), 57–64.

Shen, C., and Lemmin, U. (**1999**). "Application of an acoustic particle flux profiler in particle-laden open-channel flow," J. Hydraul. Res. **37**(3), 407–419.

Smyth, C., Hay, A. E., and Zedel, L. (**2002**). "Coherent Doppler Profiler measurements of near-bed suspended sediment fluxes and the influence of bed forms," J. Geophys. Res.: Oceans **107**(C8), 19-1–19-20, https://doi.org/10.1029/2000JC000760.

Spinewine, B., Capart, H., Fraccarollo, L., and Larcher, M. (**2011**). "Laser stripe measurements of near-wall solid fraction in channel flows of liquid-granular mixtures," Exp. Fluids **50**, 1507–1525.

Strutt, J. W., and Rayleigh, J. W. S. B. (**1877**). *The Theory of Sound* (Macmillan, London), Vol. 1.

Sumer, B. M., Kozakiewicz, A., Fredsøe, J., and Deigaard, R. (**1996**). "Velocity and concentration profiles in sheet-flow layer of movable bed," J. Hydraul. Eng. **122**(10), 549–558.

Thomas, R. E., Schindfessel, L., McLelland, S. J., Creëlle, S., and De Mulder, T. (**2017**). "Bias in mean velocities and noise in variances and covariances measured using a multistatic acoustic profiler: The Nortek Vectrino Profiler," Meas. Sci. Technol. **28**(7), 075302.

Thorne, P. D., and Hanes, D. M. (**2002**). "A review of acoustic measurement of small-scale sediment processes," Cont. Shelf Res. **22**, 603–632.

Thorne, P. D., and Hurther, D. (**2014**). "An overview on the use of back-scattered sound for measuring suspended particle size and concentration profiles in non-cohesive inorganic sediment transport studies," Cont. Shelf Res. **73**, 97–118.

van der Zanden, J., van der A, D. A., Cáceres, I., Hurther, D., McLelland, S. J., Ribberink, J. S., and O'Donoghue, T. (**2018**). "Near-bed turbulent kinetic energy budget under a large-scale plunging breaking wave over a fixed bar," J. Geophys. Res.: Oceans **123**(2), 1429–1456, http://dx.doi.org/10.1002/2017JC013411.

van der Zanden, J., van der A, D. A., Hurther, D., Caceres, I., O'Donoghue, T., and Ribberink, J. S. (**2016**). "Near-bed hydrodynamics and turbulence below a large-scale plunging breaking wave over a mobile barred bed profile," J. Geophys. Res.: Oceans **121**(8), 6482–6506, https://doi.org/10.1002/2016JC011909.

Voulgaris, G., and Trowbridge, J. H. (**1998**). "Evaluation of the acoustic Doppler velocimeter (ADV) for turbulence measurements," J. Atmos. Ocean. Technol. **15**(1), 272–289.

Zedel, L. (**2008**). "Modeling pulse-to-pulse coherent Doppler sonar," J. Atmos. Ocean. Technol. **25**(10), 1834–1844.

Zedel, L., and Hay, A. E. (**1999**). "A coherent Doppler profiler for high-resolution particle velocimetry in the ocean: Laboratory measurements of turbulence and particle flux," J. Atmos. Ocean. Technol. **16**(8), 1102–1117.

Zedel, L., and Hay, A. E. (**2002**). "A three-component bistatic coherent Doppler velocity profiler: Error sensitivity and system accuracy," IEEE J. Ocean. Eng. **27**(3), 717–725.

Zedel, L., Hay, A. E., Cabrera, R., and Lohrmann, A. (**1996**). "Performance of a single-beam pulse-to-pulse coherent Doppler profiler," IEEE J. Ocean. Eng. **21**(3), 290–297.

Zedel, L., Hay, A. E., Wilson, G. W., and Hare, J. (**2021**). "Pulse coherent Doppler profiler measurement of bedload transport," J. Geophys. Res. Earth Surf. **126**(4), e2020JF005572, https://doi.org/10.1029/2020JF005572.

J. Acoust. Soc. Am. **155** (4), April 2024

Fromant *et al.* 2835